NORTHWEST AFRICA (NWA) 12563 and ungrouped C2 chondrites: Alteration styles and relationships to asteroids

R.H. Hewins, P.-M. Zanetta, B. Zanda, C. Le Guillou, J. Gattacceca, C. Sognzoni, S. Pont, L. Piani, T. Rigaudier, H. Leroux, et al.

NWA 12563 and ungrouped C2 chondrites: Alteration styles and relationships to asteroids

R. H. Hewins[a,b*], P.-M. Zanetta[c1], B. Zanda[a,d], C. Le Guillou[c], J. Gattacceca[e], C. Sognzoni[e], S. Pont[a], L. Piani[f], T. Rigaudier[f], H. Leroux[c], R. Brunetto[g], R. Maupin[g], Z. Djouadi[g,i], S. Bernard[a], D. Deldicque[h], V. Malarewicz[a], Z. Dionnet [i], A. Aléon-Toppani[g], A. King[j], F. Berendics[j]

[a]IMPMC, Sorbonne Univ., MNHN, UPMC Paris 06, UMR CNRS 7590, 75005 Paris, France.
[b]EPS, Rutgers Univ., Piscataway, NJ 08854, USA.
[c]Univ. Lille, CNRS, INRAE, Centrale Lille, UMR 8207 - UMET - Unité Matériaux et Transformations, F-59000 Lille, France.
[d]IMCCE, Observatoire de Paris, CNRS UMR 8028, 75014 Paris, France.
[e]CNRS Aix-Marseille Univ., IRD, INRAE, CEREGE, Aix-en-Provence, France.
[f]Univ. Lorraine and CNRS, CRPG, UMR 7358, Vandoeuvre-lès-Nancy, 54501, France.
[g]Université Paris-Saclay, CNRS, Institut d'Astrophysique Spatiale, 91405 Orsay, France.
[h]Labo. de Géologie, Ecole Normale Supérieure, 75231 Paris, France.
[i]Università degli Studi di Napoli Parthenope, Dip. di Scienze e Tecnologie, CDN IC4, I-80143 Naples, Italy.
[j]Synchrotron SOLEIL, L'Orme des Merisiers Saint-Aubin, Gif-sur-Yvette, France.
[1]present address Lunar and Planetary Laboratory, University of Arizona, Tucson AZ, USA.

*Corresponding author. Email hewins@scarletmail.rutgers.edu, +33 6 16 21 29 91 & +33 1 4709 3769

Submitted to GCA December, 2020.

Abstract—Many asteroids in the main belt have spectra like those of Mighei-type CM chondrites, but some Near Earth Objects (NEO) resemble less well known types of C2 chondrite. Northwest Africa (NWA) 12563, a new find with affinities to C2 chondrites, could help us understand the differences between observations of CM2 chondrites and bodies that are currently being studied by the Hayabusa 2 and Osiris-Rex space missions. NWA 12563 contains 14% chondrules supported by 86% fine grained matrix consistent with CM2 chondrites, but differs in other respects. In both matrix and chondrules, olivine is unaltered and pyroxene shows incipient alteration. Metal in chondrules is pseudomorphed by serpentine, and mesostasis is replaced by serpentine- saponite and chlorite. Many Type I chondrules have gerrymandered shapes resulting from fracturing and selective metal replacement. Type II porphyritic chondrules are clusters of phenocrysts set in matrix-like material. Type II chondrules may be kinked and partially disbarred. The matrix of NWA 12563 is characterized by the absence of tochilinite-cronstedtite intergrowths. It contains hydrated and oxidized amorphous silicate ($Fe^{3+}/\sum Fe$ ~75%) richer in magnesium than in other chondrites (with embedded sulfides). Serpentine-saponite is also present, as well as abundant framboidal magnetite.

NWA 12563 has similarities to a number of ungrouped magnetite-rich and ^{18}O-rich chondrites (Bells, Essebi, Niger I, WIS 91600, Tagish Lake, Dho 1988 and MET 00432) that we call C2-ung1, as opposed to ^{18}O-poor C2-ung2 chondrites. The oxygen isotopic composition coupled with a magnetic susceptibility of $\log \chi = 4.67$ places NWA 12563 with these ungrouped chondrites in a cluster distinct from CM2 chondrites. NWA 12563 is closest to WIS 91600 among the C2-ung1 chondrites in alteration style and light element compositions. WIS 91600, however, has suffered light thermal metamorphism, suggesting that NWA 12563 might represent its altered but unheated precursor material within the same parent body if it were zoned. The average Vis-NIR spectrum of NWA 12563 matches the asteroid taxonomic class K and resembles that of CO3 Frontier Mountain (FRO) 95002, but its spectra range from very “red” in dark matrix areas and very “blue” in magnetite-rich areas. The average MIR spectrum shows features indicating phyllosilicates, aliphatic CH compounds, hydrated silicates, and olivine. It is significantly different from those of other chondrites including FRO 95002, and closest to Bells (from which it differs in carbon isotopic composition) and WIS91600. The variety of mineralogical, chemical and isotopic properties among C2-ung1 chondrites requires several different parent bodies. However, the high abundance of magnetite common to this cluster of ungrouped chondrites, and to a lesser extent CI chondrites, indicates that they should be considered as possible material from Bennu, which has an 18 μm magnetite signal in its spectrum not seen in the CM2 chondrites (Hamilton et al., 2019).

1. INTRODUCTION

C-complex asteroids form a major fraction of the bodies in the main asteroid belt at ~3-4 AU (Burbine, 1998; Vernazza and Beck, 2017, Vernazza et al., 2017), and were probably formed beyond the snow line whether this was in the inner or outer solar system (Warren, 2011; Walsh et al., 2011). The largest category, the Ch- and Cgh-types, comprises ~70 asteroids in the main belt, as well as family members, and is well matched spectrally by CM carbonaceous chondrite meteorites (Vernazza et al., 2017). As the only well-established meteorite analogs of C-complex asteroids, the geologic history of the CMs is particularly important. They contain high temperature particles, including chondrules, and fine-grained hydrated matrix reflecting processes in the disk and in asteroidal bodies. The source of the ice accreted into asteroids and the timing and conditions of aqueous alteration are both key issues in early solar system history. From the CM group we have learned that water from isotopically different inner and outer solar system reservoirs was present (Piani et al., 2018).

Many other types of asteroids have not been definitively matched with chondrite groups as yet. D-type asteroids were proposed to be related to the Tagish Lake C2-ung chondrite (Hiroi et al., 2001) yet Vernazza and Beck (2017) report that they lack the hydrated minerals found in Tagish Lake. B-type asteroid spectra can be matched by CI chondrite provided that magnetite is added (Yang and Jewett, 2010). Of the two NEO asteroids recently visited by spacecraft, Ryugu is a Cb asteroid (Sugita et al., 2019) similar spectrally to some C2-ung and CY chondrites that experienced heating (Tonui et al., 2014; Kitazato, 2019; King et al., 2019). The other, Bennu, is classified as a B-type asteroid (Clark et al. 2011) and may be composed of C2 rather than CM2 material (de Léon et al., 2018; Tachibana et al., 2019; Kitazato et al, 2019; Lauretta et al., 2019; Hamilton et al., 2019). Deciphering the different properties and histories of rare ungrouped and anomalous C meteorites (C2-ung and CM-an) which have some similarities to CM2 and some to CI chondrites, and vary among themselves, could lead to a broader basis for interpreting C-complex and other asteroids.

Here we report on a new carbonaceous chondrite NWA 12563 which contains an unusual combination of mineral assemblages consistent with a different alteration history from CM2 meteorites. Its matrix contains abundant magnetite and serpentine-saponite rather than the cronstedtite and tochilinite characteristic of CM2 chondrites. Its similarities to several magnetite-rich C2-ung chondrites that have higher $\delta^{18}O$ than CM2 chondrites (Greenwood et al., 2020) potentially illuminate the geological histories of the other asteroid groups. This work is timely, in view of current missions to explore NEO asteroids Ryugu and Bennu (Tachibana et al., 2019; Kitazato et al, 2019; Lauretta et al., 2019; Hamilton et al., 2019).

2. ANALYTICAL METHODS

2.1. Oxygen Isotope analysis

Three-oxygen-isotope analysis was carried out at the Stable Isotopes Laboratory of CEREGE. We analyzed one 1.5 mg aliquot of a powdered 20 mg bulk sample washed in HCl (1N) for 2 hours. Molecular oxygen was extracted using laser fluorination. The aliquot was heated with a 30 W CO_2 IR laser in the presence of 100 mbar of BrF_5. The released gas was purified through two cryogenic nitrogen traps and one heated KBr trap. Molecular oxygen was trapped for 10 mn in a molecular sieve cooled at -196°C. The gas was then expanded at 100°C and passed through a molecular sieve cooled at -114°C slush for 5 mn to refreeze possible interfering gases. The gas was then trapped again for 5 mn in the molecular sieve cooled at -196°C, then expanded again at 100°C directly into the bellow of a dual-inlet Thermo-Finnigan Delta Plus mass spectrometer.

The isotopic compositions are expressed in standard δ-notation, relative to Vienna standard mean ocean water (VSMOW): $\delta^{18}O = (^{18}O/^{16}O)_{sample} / (^{18}O/^{16}O)_{VSMOW} - 1$ and $\delta^{17}O = (^{17}O/^{16}O)sample / (^{17}O/^{16}O)_{VSMOW} - 1$ (expressed in ‰), $\Delta^{17}O$, also expressed in ‰, is defined as $\delta^{17}O - \lambda \times \delta^{18}O$. For comparison with literature data, we use $\lambda = 0.52$. Measured $\delta^{18}O$ and $\delta^{17}O$ values of the samples were corrected daily using the laboratory quartz standard itself calibrated against the international standard NBS28 ($\delta^{18}O = 9.60$ ‰, $\delta^{17}O = 0.52 \times \delta^{18}O = 4.992$ ‰). Reproducibility (1 sigma) of the quartz laboratory standard are 0.119‰ for $\delta^{18}O$, 0.061‰ for $\delta^{17}O$, and 0.024‰ for $\Delta^{17}O$ (n = 63) with a $\Delta^{17}O$ (defined as $\delta^{17}O - \lambda \times \delta^{18}O$ with $\lambda = 0.52$) of -0.015 ± 0.024‰.

2.2. Magnetic methods

Hysteresis measurements were performed on a 160.2 mg bulk sample at CEREGE with a Princeton Micromag Vibrating Sample Magnetometer with a maximum applied field of 1 T and a sensitivity of ~$5x10^{-9}$ Am^2. The analysis of hysteresis loops provided the ratio of saturation remanent magnetization (M_{RS}) to saturation magnetization (M_S) and the coercive force (BC). High field susceptibility (χ_{HF}) was determined by a linear fit for applied fields > 0.9 T of the hysteresis loops. Remanent coercive force (B_{CR}) was determined by DC back field experiments performed with the VSM. Low-temperature remanence measurements were performed with an MPMS from Quantum Design®. This instrument has a moment sensitivity of 10^{-11} Am^2. The low field specific susceptibility (χ in m^3/kg) and its evolution with temperature were measured using Agico MFK1 apparatus with sensitivity of $5x10^{-13}$ m^3, operating at 200 A/m and a frequency of 976 Hz, equipped with a CS3 furnace and a CSL cryostat. Isothermal remanent magnetizations (IRM) were imparted using a pulse magnetizer from Magnetic Measurements. Thermal demagnetization was performed using an MMTD furnace, under argon atmosphere above 250 °C. For most samples, we measured the S ratio that is the IRM obtained after applying a 3 T field and then a back field of 0.3 T normalized to the IRM acquired in 3 T. Remanence measurements were performed with a SQUID cryogenic magnetometer (2G Enterprises, model 755R, with noise level of 10^{-11} Am^2). All magnetic measurements were performed at CEREGE (Aix-en-Provence, France), with the exception of MPMS measurements (at IPGP, Paris, France). The magnetic susceptibility of NWA 12563 was measured on samples weighing 13.7 g and 160.2 mg. The magnetic properties for the CY chondrite Dhofar 2066 were measured on 2.69 g for susceptibility and 250 mg for MS.

2.3. Scanning Electron Microscopy

A sample of NWA 12563 was cut at the Institut de Minéralogie, de Physique des Matériaux, et de Cosmochimie (IMPMC), Muséum National d'Histoire Naturelle (MNHN), to prepare a polished section for study using reflected light microscopy, scanning electron microscopy (SEM), and electron probe micro analysis (EPMA). A back-scattered electron (BSE) map and images of selected regions were made at MNHN using a Tescan VEGA II LSU SEM in conventional mode (mainly 15keV, <20nA and 15.4 mm working distance). Minerals were characterized on the MNHN SEM with an SD^3 (Bruker) EDS detector.

Images were acquired at the Ecole Normale Supérieure Paris using a ZEISS ZIGMA field emission gun (FEG) SEM equipped with an Oxford Instrument X-MAX EDS detector. The accelerating voltage was 15 keV with a working distance of 9 to 10 mm (in backscattered mode). The Inca Software (Oxford Instruments) was used for qualitative analysis and mapping by dispersive energy spectra (EDS). For high resolution images we used 5 keV and a working distance between 2 and 3mm.

Hyperspectral maps and high resolution images of chondrite matrix were acquired using a FEG-SEM JEOL JSM-7800F LV at the University of Lille equipped with an EDX/EBSD Aztec system from Oxford Instruments and a silicon drift detector (SDD XMaxN) of 80 mm^2. The sample has been studied

using hyperspectral maps with 1024 by 768 pixels corresponding to a region of 250 µm by 192 µm. A representative matrix region of 125 µm by 96 µm using a resolution of 512*384 pixels is discussed below. A working distance of 10 mm and an energy range of 10 keV for 2048 channels (5ev per channel) were used. During acquisition, a drift correction was applied, based on the corresponding BSE image. The phase map was based on a simplified version of the ACADEMY methodology (Analyzing the Composition, the modal Abundance and the Density using Electron MicroscopY; Zanetta et al., 2019) using XMapTools software (Lanari et al., 2014). We used a BSE image mosaic and the Qgis® software to estimate the chondrule and matrix proportions.

2.4. Transmission Electron Microscopy

We prepared six electron transparent sections by the focused ion beam (FIB) technique using an FEI Strata dual beam 235 at IEMN, University of Lille. The sizes of the FIB sections were typically ~200 μm^2 and 150 nm thick. The FIB sections were studied with an FEI Tecnai G2-20 TWIN (LaB6, 200 kV) equipped with an EDAX energy dispersive spectrometer (EDS) and a Titan Themis, at 300 kV using a four quadrant, windowless, super-X SDD system. K-factors for O, Fe, Mg, Al, S, Ca, and K were experimentally acquired on standards (fayalite, forsterite, basalt and rhyolite, serpentine, wollastonite and pyrite). Compositional data were deduced from elemental mapping after post-acquisition processing of data cubes using Hyperspy (De la Peña, et al., 2017; Zanetta et al., 2019).

2.5. Electron Microprobe Analysis

All quantitative mineral analyses were made by wavelength-dispersive spectrometry on the Cameca SXFive electron microprobe at the Université Paris VI, mainly using 15keV and 10 nA, with a focused beam or small rasters. We used silicate, oxide and phosphate standards, and monitored conditions with Astimex chlorite, San Carlos olivine and Eagle Station olivine internal standards. K_α lines were measured on standards using diffracting crystals as follows: Na, albite LTAP; Mg olivine LTAP; Si olivine TAP; Al orthoclase LPET; K orthoclase LTAP; Ca, diopside LPET; Ti, $MnTiO_3$; Cr, Cr_2O_3 PET; Mn, $MnTiO_3$LLIF;Fe, FeS_2 LLIF; F, apatite LTAP; P, apatite LPET; Cl, scapolite PET; F (sic) CaF2 TAP; Ni NiO LLIF. The counting time was 10 sec for peaks and backgrounds, increased to 20 or 60 sec for some minor elements.

2.6. Scanning Transmission X-ray Microscopy (STXM)

X-ray Absorption Near Edge Structure (XANES) data were collected using a scanning transmission X-ray microscope on the HERMES STXM beamline (Belkhou *et al.*, 2015; Hitchcock, 2017) at the synchrotron SOLEIL. Optical elements were exposed to a flow of O_2 to remove carbon contamination from the beamline. Energy calibration was performed using the 3p Rydberg peak of gaseous CO_2 at 294.96 eV. X-rays are focused on a 30 nm probe using a Fresnel zone plate. Alignment of images of stacks and extraction of XANES spectra were done using the aXis2000 software. We collected images at energy increments of 0.1 eV over the carbon absorption range (282–295 eV) with a dwell time of ~ 1 ms per pixel to prevent irradiation damage, and at energy increments of 0.2 eV over the Fe-L edge absorption range (705-713 eV). The C-XANES spectra were normalized to the carbon quantity, deconvolved, and quantified following the method developed by Le Guillou et al. (2018). The $Fe^{3+}/\sum Fe$ ratio was obtained based on the calibration developed by Bourdelle et al. (2013) and Le Guillou et al. (2015).

2.7. Raman spectroscopy

Raman spectroscopy was used to document the degree of structural organization of the carbonaceous material. Raman data were obtained on a freshly fractured surface, at room temperature,

using a Renishaw INVIA spectrometer (IMPMC, Paris, France) in a confocal configuration equipped with a 514.5-nm wavelength 50-mW Modulaser Ar laser. The configuration used yields a horizontal resolution of ~ 1 μm for a laser power delivered at the sample surface below 500 μW, thereby preventing irreversible thermal damage (Beyssac et al., 2003; Bernard et al., 2008).

2.8 Hydrogen, nitrogen and carbon analysis

The measurements of the carbon and nitrogen concentrations and carbon isotopic composition (reported as $\delta^{13}C$ calculated against the standard Pee Dee Belemnite with a $^{13}C/^{12}C$ ratio of 0.0112372) were performed on-line using the Thermo Scientific EA IsoLink - deltaV IRMS System at CRPG laboratory (Nancy, France) using a 2-mg aliquot of the meteorite powder. The precision of the measurement for nitrogen concentration, carbon concentration and isotopic composition are estimated to be 30 %, 2 %, and 2 ‰, respectively.

The measurements of the hydrogen concentration and isotopic composition were performed on-line using the Thermo Scientific EA IsoLink - deltaV IRMS System at CRPG laboratory (Nancy, France) according to the procedure detailed in Lupker et al. (2012). For hydrogen measurement, the meteorite was crushed into powder and two 2-mg-aliquots were loaded in tin capsules and degassed at 120°C under vacuum for 48h to minimize the contribution of adsorbed atmospheric water (Lupker et al., 2012; Vacher et al., 2016, 2020). The hydrogen isotopic composition is expressed as δD (‰) relative to Standard Mean Ocean Water (SMOW): $\delta D = (D/H_{sample} / D/H_{SMOW} - 1) \times 1000$, where SMOW represents the reference value of terrestrial oceans ($D/H_{SMOW} = 155.76 \times 10^{-6}$). The reproducibility estimated on reference materials is better than 10% (2σ) for the concentration of H and 0.5×10^{-6} for D/H (or 5‰ for δD).

2.9 X-ray computed tomography (X-CT)

X-CT characterization was performed at the synchrotron X-ray beamline PSICHE at SOLEIL synchrotron (France). The measurement was performed with a parallel monochromatic beam of 25 keV and with an exposure time of 500 ms per each projection. A matrix sub volume with a volume of 830 * 1500 * 700 μm was studied in detail. We measured 5900 2D projections of the linear attenuation coefficient (LAC) to reconstruct the LAC variations in 3D, with a final voxel size of ~0.87 μm. Post-processing 3D reconstruction was achieved using the Python library Tomopy (Gursoy et al. 2014). The reconstruction was performed using PyHST2 (Mirone et al., 2014). Detection of pores and iron-rich phases was then performed thanks to a threshold segmentation (Dionnet et al. 2020), and the study of the structures' shape was conducted with Quant3D (Ketcham et al. 2005).

2.10 Visible-NIR micro-spectroscopy

Visible and near-IR diffuse reflectance micro-spectroscopy was performed in a clean room at IAS-Orsay (France), using a Vis–NIR (0.4-1.1 μm) grating spectrometer Maya2000 Pro (OceanOptics) with 4.5 nm spectral resolution coupled to a macroscope (Leica Z16 APO). The sample is unilaterally illuminated at ~45° incident angle by a 1000 μm diameter fiber which is coupled to a halogen source. A collecting optical fiber is positioned orthogonally to the sample to collect the light diffused by the sample at 0° angle. By changing the magnification and/or the diameter of the collection fiber it is possible to adjust the collection spot down to about 7 μm. We also measured spectra in a macroscopic configuration, using a collection spot of about 1 mm. In both cases, reference spectra were collected with respect to a 99% Spectralon standard (from Labsphere). Spectra were measured at 20 different azimuth angles and averaged to take into account potential effects of the observation geometry. See Maupin et al. (2020) for more details.

2.11 IR micro-spectroscopy

Mid-IR reflectance spectra and maps for polished sections of NWA 12563, Bells, and Essebi were collected at the SMIS beamline of the SOLEIL synchrotron (France) using an a Nicolet Continuum XL microscope (Thermo Fisher) equipped with a 50 × 50 μm2 liquid-nitrogen-cooled MCT/A detector (narrow-band, 650 cm^{-1} cut-off) and a 32× NA 0.65 Schwarzschild objective. The microscope was coupled to a Nicolet 5700 spectrometer (Thermo Fisher) equipped with a Michelson interferometer and a KBr beamsplitter. The IR source was the external synchrotron light source and the aperture was set to produce an analytical spot of 10-20 μm on the focal plane. The spectral resolution was either 4 or 8 cm^{-1}, and at least 256 scans per spectrum were accumulated. Before each analysis, a background spectrum was acquired on a gold mirror standard. The average MIR spectrum of NWA 12563 was obtained by averaging more than 650 individual spectra obtained at different locations of the meteorite. All the spectra were taken from areas larger than 500x500 μm^2.

Additional MIR hyperspectral imaging data of NWA 12563, Bells, and Essebi were acquired with an Agilent Cary 670/620 micro-spectrometer equipped with a 128x128 pixel Focal Plane Array detector (3900-800 cm^{-1}), installed at SMIS, using the internal globar source at 8 cm^{-1} spectral resolution. The IR maps were acquired in reflectance geometry, with respect to gold references, using a x15 objective which produces a 5.5 μm pixel size on the focal plane. More details about the setup are described by Brunetto et al. (2018) and Noun et al. (2019).

The far-IR (FIR, 700–100 cm^{-1} or 14–100 μm) spectra of NWA 12563, Bells, and Essebi were acquired at SMIS using a NicPlan microscope, coupled to an iS50 FTIR spectrometer (Thermo Fisher) operating in confocal reflection geometry, with respect to gold references, using a bolometer detector (boron doped silicon, 4.2 K cooled, Infrared Laboratories) and a solid-state Si beam splitter. The spectral resolution was 4 cm^{-1} and the spectral sampling 0.5 cm^{-1}. We mapped mm-sized areas using variable spot sizes of 80-300 μm in diameter per spectrum. The various spectra were then averaged to finally produce average spectra representative of the meteorites. Thus, we averaged the small scale heterogeneity of the chosen chondrites. The bolometer also allowed us to acquire data in the 750–1050 cm^{-1} (13.3–9.52 μm) range. Although noisy, this additional spectral range proved to be useful to properly combine spectral ranges obtained with different detectors. The FIR spectra were scaled to match the MIR spectra in the overlapping region, similarly to what was reported by Brunetto et al. (2020) for Tagish Lake, Murchison, Alais, Mighei, Paris, Allende, Lancé, and Frontier Mountain 95002 meteorites. In the case of NWA 12563, we also acquired additional MIR spectral maps using another Nicolet Continuum microscope at SMIS, equipped with a 250 μm liquid-nitrogen-cooled MCT/B detector (450 cm^{-1} cut-off) and a 15× Schwarzschild objective, to better combine the MIR and the FIR spectra, and to focus on the IR spectral signature of magnetite in one particular area of the meteorite.

The combined MIR-FIR spectra were finally baseline-corrected using a convex hull. The baseline correction was performed to focus on the position and shape of the IR spectral bands, and to allow comparison with emissivity IR remote sensing data of asteroids whose continuum is usually taken into account and removed in the thermal model of the spectral energy distribution (Emery et al., 2006).

3. RESULTS

3.1 Chondrite properties

3.1.1 Petrography

This chondrite with 14% chondrules supported by 86% fine grained matrix and accretionary chondrule rims is seen in Fig. 1a. The abundances were determined by using the image analysis program Qgis© and the term chondrule here includes complete chondrules, large chondrule fragments, and clusters or aggregates of phenocrysts (Fig. 1b). About 84% of the chondrules are Type I and about 16% Type II, while a large Al-rich chondrule is included with CAI and AOA in Fig. 1b as refractory material. Fig. 1b shows that only 46% of the chondrules have complete or partial fine-grained compact accretionary rims. The chondrule abundance is at the low end of the normal range for CM chondrites but the matrix includes isolated grains (tens of microns in size) likely derived from chondrules. Chondrule size ranges from 15 μm to 2 mm, with many smaller ones being fragments or disrupted loose crystals. Olivine (unaltered) is much more abundant than pyroxene, occurring both in Type I and II chondrules, and as crystal clasts in the matrix. Pyroxene (Mg-pigeonite and inverted protopyroxene) is found in some large chondrules. Amoeboid olivine aggregates and spinel-rich aggregates are rare.

The matrix is fine-grained (<100 nm to a few microns), with phyllosilicates, easily identifiable at the SEM scale by their fibrous nature, and amorphous silicate. It contains abundant magnetite (as framboids, spherules and plaquettes), plus pentlandite, troilite, sulfide-oxide aggregates, minor carbonate aggregates, but no scabby patches of tochilinite intergrown with cronstedtite. The matrix has a heterogeneous appearance (Fig. 1) with BSE intensity fluctuations due to the local variations in magnetite size distribution and abundance: bright areas have many small clusters of fine framboids while dark areas have scattered coarse framboid groupings. The matrix sample examined by X-CT with ~0.87 μm voxels contains a few crystal clasts up to 150 μm in size and is very compact, with a very low porosity of 0.7± 0.5% (Fig. S1a). The pores are anisotropic with average A = 5.6, the slight elongation meaning the meteorite has probably experienced weak shocks. The fractures are possibly related to shock or dehydration (Fig. S1b). At the scale of X-CT measurements, magnetite is fairly uniformly distributed in the three dimensions and its abundance in this chip is 5.8% (Fig. S1c).

Fig. 1. (a) BSE image of polished section of NWA 12563. Dark grey is magnesian olivine, medium grey is pyroxene and phyllosilicate, light grey is ferroan olivine, sulfide and magnetite, with a continuous grey serpentine-rich matrix. (b)The corresponding map is based on the BSE image.

3.1.2 Oxygen Isotopes

The oxygen isotopic composition of NWA 12563 is $\delta^{18}O$=12.61‰ and $\delta^{17}O$=5.26‰, with $\Delta^{17}O$ of -1.33 (linearized, slope 0.5247, analytical uncertainties 0.08‰, 0.12‰, 0.03‰ respectively). It plots at the upper end of the CO-CM trend line (Fig. 2), very close to the C2-ung Essebi (Rowe et al., 1994). We compare $\delta^{18}O$ values, mineralogy and magnetic susceptibility with those of other chondrites of interest in section 7.2 and propose to call those with higher $\delta^{18}O$ values C2-ung1 and those with lower $\delta^{18}O$ values C2-ung2.

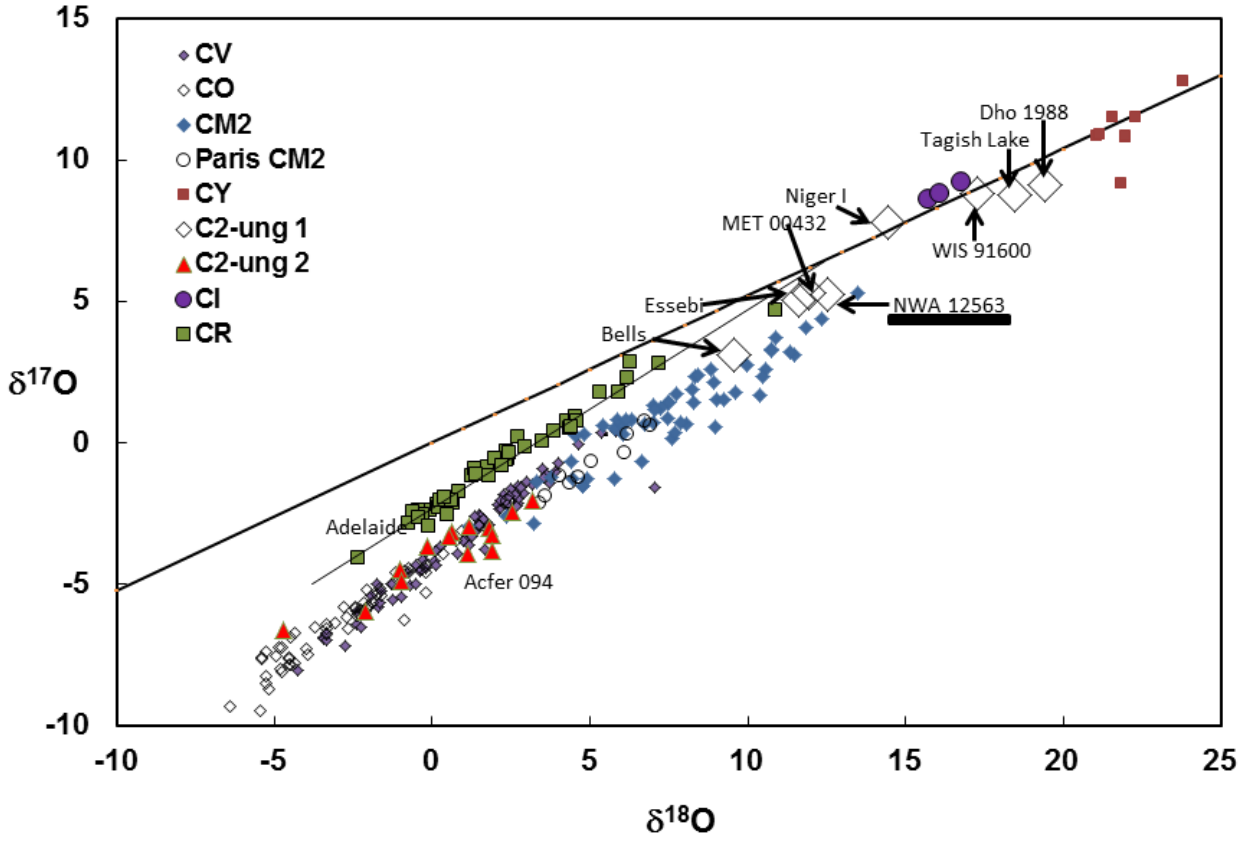

Fig. 2. Oxygen isotopic composition of NWA 12563 compared to those of other carbonaceous chondrites (Greenwood et al, 2020). Ungrouped and anomalous C2 chondrites occur in two clusters separated by typical CM2 chondrites.

3.1.3 Magnetic Properties

Thermomagnetic measurements reveal a sharp and reversible magnetic transition at 585°C (Fig. 3a), which is the Curie temperature of magnetite. Magnetite is thus the ultra-dominant ferromagnetic mineral in this meteorite. The presence of magnetite is confirmed by the magnetic Verwey transition observed at -153°C in the low temperature magnetic measurements (Fig. 3b). The magnetic susceptibility values of log χ = 4.67 (where χ is in 10^{-9} $m^3.kg^{-1}$) indicate small scale homogeneous distribution of magnetite. This value is close to the values for Bells, Essebi, and Niger I C2-ung at 4.82, 4.85, and 4.89 respectively, and higher than all except 4 of 52 CM chondrites that give an average logχ = 3.90±0.43 (Rochette et al., 2008). Saturation magnetization M_s is 6.26 Am^2/kg, corresponding to 6.80 wt% of magnetite. This is similar to the value for Niger I, M_S=9.85 Am^2/kg that we measured on four samples totaling 2.55 g. For comparison, the

363 average M_S for CM chondrite falls is 1.01±0.55 Am^2/kg (N=9), data from Cournède et al. (2015) and new
364 data from this study for Boriskino, Murchison, Pollen, Santa Cruz (M_S=1.76, 0.671, 0.234, 1.45 Am^2/kg,
365 measured on total masses of 31, 944, 20, 221 mg, respectively. The magnetite content of NWA 12563 is
366 thus more than five times higher than in the average CM chondrite.
367
368 In more detail, IRM acquisition is not completed around 300 mT (Fig. 3c), as should be the case if
369 magnetite was the only ferromagnetic mineral. IRM is still acquired up to 1 T (the maximum field used in
370 our experiments), which implies that a high coercivity ferromagnetic mineral is present in addition to
371 magnetite. This is confirmed by the S_{-300} ratio (ratio of SIRM superimposed with a back-field isothermal
372 remanent magnetization at 300 mT over SIRM) of -0.86, also indicative of the presence of a high-coercivity
373 mineral in addition to magnetite. Fe,Ni metal is unlikely because it usually has a low coercivity except in
374 the form of tetrataenite in the cloudy zone structure (Gattacceca et al., 2014), or as kamacite grains in dusty
375 olivines (Lappe et al. 2011)), none of which are observed in NWA 12563, and also because the magnetic
376 susceptibility is negligible above 585°C (Fig. 3a). Pyrrhotite is a candidate because it has much lower
377 susceptibility than magnetite so a minor pyrrhotite abundance compared to magnetite would go totally
378 unnoticed in the thermomagnetic experiments.

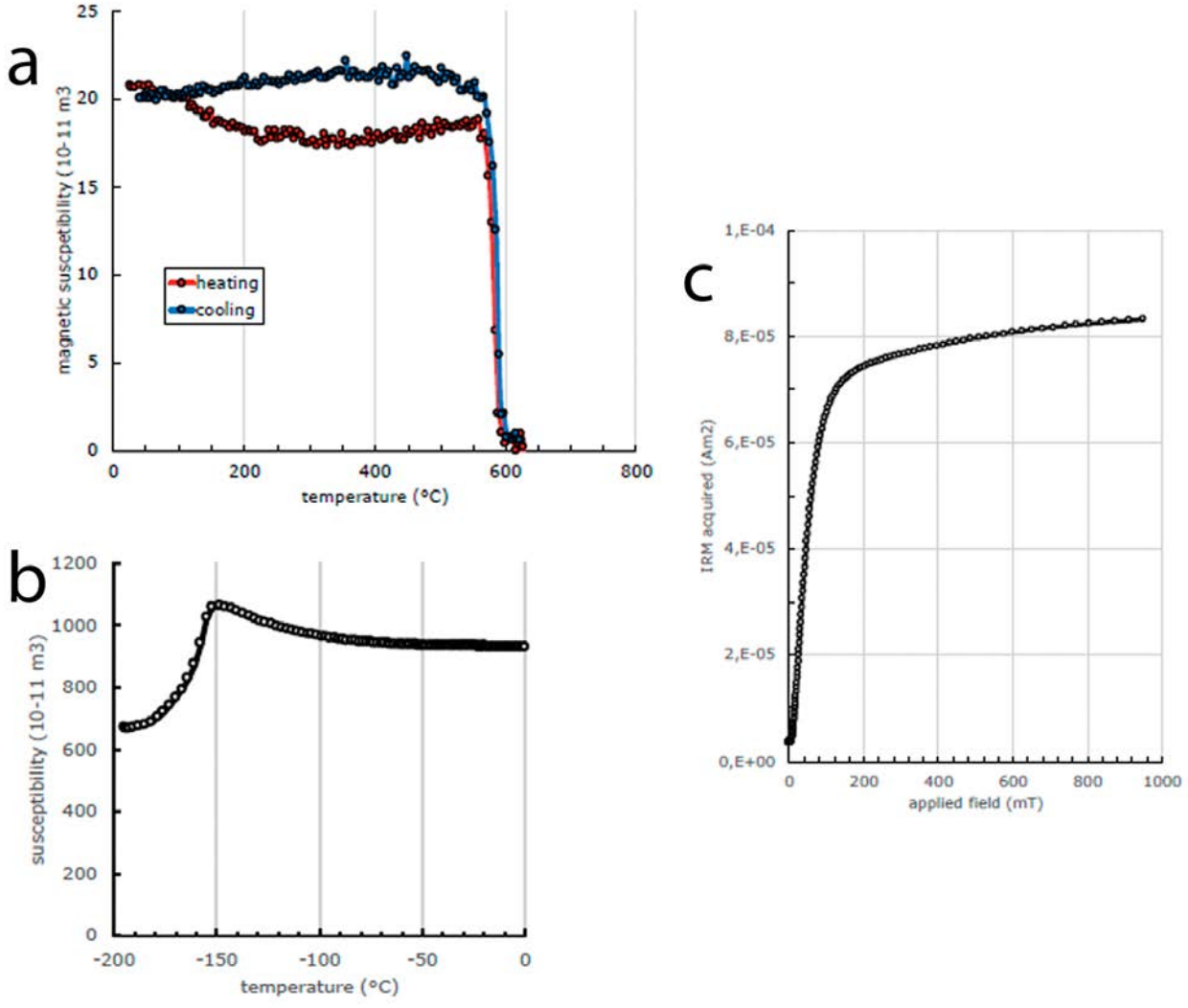

379
380
381

Fig. 3. (a) Thermomagnetic measurements show the presence of magnetite by the magnetic transition at 585°C, its Curie temperature. (b) The magnetic Verwey transition observed at -153°C confirms the presence of magnetite. (c) IRM acquisition is incomplete at 300 mT (Fig. 3c), probably due to pyrrhotite.

3.1.3 Hydrogen, nitrogen, and carbon

The carbon concentration of NWA 12563 is 2.13 wt.% C, with a $\delta^{13}C$ of -12.2 ‰, and the nitrogen content is 0.095 wt.% N. The hydrogen concentrations measured for the two aliquots after degassing at 120°C correspond to 0.73 and 0.72 wt.%, equivalent to 6.6 and 6.5 wt.% H_2O, with an isotopic composition δD of -57.7 and -57.6 ‰, respectively. These values are typical of normal CM chondrites (Alexander et al., 2012; Vacher et al., 2016; Vacher et al., 2020), although the hydrogen concentrations are in the lower end of the concentration range measured for CM chondrites (from ~5 to 13 wt.% H_2O). The hydrogen concentrations and C/H ratios (C/H at.% = 0.24) measured for NWA 12563 are close to the one measured for the ungrouped chondrites Tagish lake, Bells and Essebi (5.0 to 8.6 wt.% H_2O and C/H at.% from 0.15 to 0.45; Alexander et al., 2012). These values might also resemble to the one of heated CM-chondrites (Alexander et al., 2012), though our studies of matrix (below) show no evidence of dehydration.

3.2 High temperature materials

3.2.1 Refractory Inclusions

Refractory inclusions are rare (~0.2%). They include spinel-rich inclusions in which other primary phases have been destroyed, except for accessory perovskite (Fig. 4a), and amoeboid olivine aggregates (AOA) with accessory Ni-rich schreibersite (Fig. 4b).The olivine in AOA overlaps in composition with olivine in chondrules and isolated grains, but Fig. 5 shows that it is closer on average to pure forsterite in minor elements as well as Fe and Mg ($Fo_{99.3\pm0.7}$ vs $Fo_{98.9\pm0.7}$). Its concentrations of Fe and minor elements resemble those of AOA olivine in primitive chondrites like Acfer 094 (Krot et al., 2004). The compositions of anhydrous silicates are given in Tables 1 and S1.

Table 1. Analyses of olivine and pyroxene from AOA, chondrules, and isolated in matrix.

Point	0bject	SiO_2	Al_2O_3	TiO_2	Cr_2O_3	FeO	MnO	MgO	CaO	Na_2O	Total	Fo/En	Fa/Fs	Wo
55	AOA	42.36	0.05	0.03	0.14	0.29	0.08	57.45	0.17	0.03	100.59	99.72	0.28	
32	AOA	43.67	0.04	bd	0.34	0.47	0.14	57.24	0.05	bd	101.96	99.54	0.46	
33	Al-rich	43.66	0.05	0.04	0.38	0.81	0.05	55.88	0.20	bd	100.85	99.19	0.81	
60	IA BO	43.18	0.12	0.08	0.10	0.37	bd	57.15	0.43	bd	101.68	99.63	0.37	
58	isolated	42.54	0.06	0.04	0.18	0.71	bd	56.52	0.42	0.02	100.47	99.30	0.70	
68	IA ch 63	42.90	0.05	0.05	0.51	1.32	0.26	56.01	0.23	bd	101.33	98.70	1.30	
51	IIA PO 51	40.57	0.05	0.03	0.40	13.16	0.26	45.78	0.13	bd	100.50	86.12	13.89	
58	IIA BO	38.84	0.06	0.01	0.42	20.71	0.27	39.78	0.19	0.01	100.49	77.40	22.60	
59	isolated	37.31	0.01	bd	0.43	28.90	0.38	33.58	0.16	bd	100.80	67.44	32.56	
52	IIA PO 51	35.49	bd	0.02	0.34	36.47	0.29	27.28	0.20	0.02	100.13	57.15	42.86	
64	isolated	34.86	0.04	bd	0.43	42.24	0.41	21.83	0.25	bd	100.49	47.95	52.05	
31	Al-rich	59.10	2.05	0.44	0.73	0.48	0.11	35.26	3.55	bd	101.84	92.60	0.71	6.70
109	IB	59.90	0.55	0.14	0.76	1.01	0.10	38.84	0.51	bd	101.85	97.66	1.42	0.92
162	IAB 158	58.23	1.03	0.15	0.59	1.61	0.03	37.94	0.47	0.07	100.14	96.83	2.31	0.86

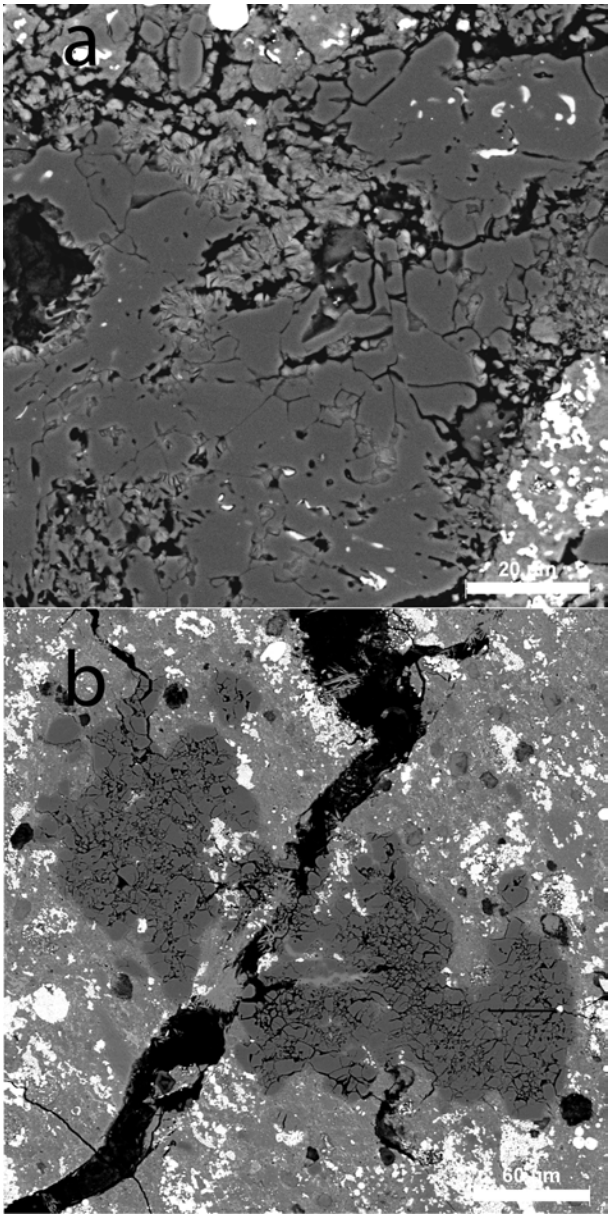

Fig. 4. (a) Spinel-rich refractory inclusion with abundant pores containing phyllosilicate, and accessory perovskite (white). (b) Amoeboid olivine aggregate with accessory Ni-rich schreibersite (arrow). Both objects are embedded in magnetite-rich matrix.

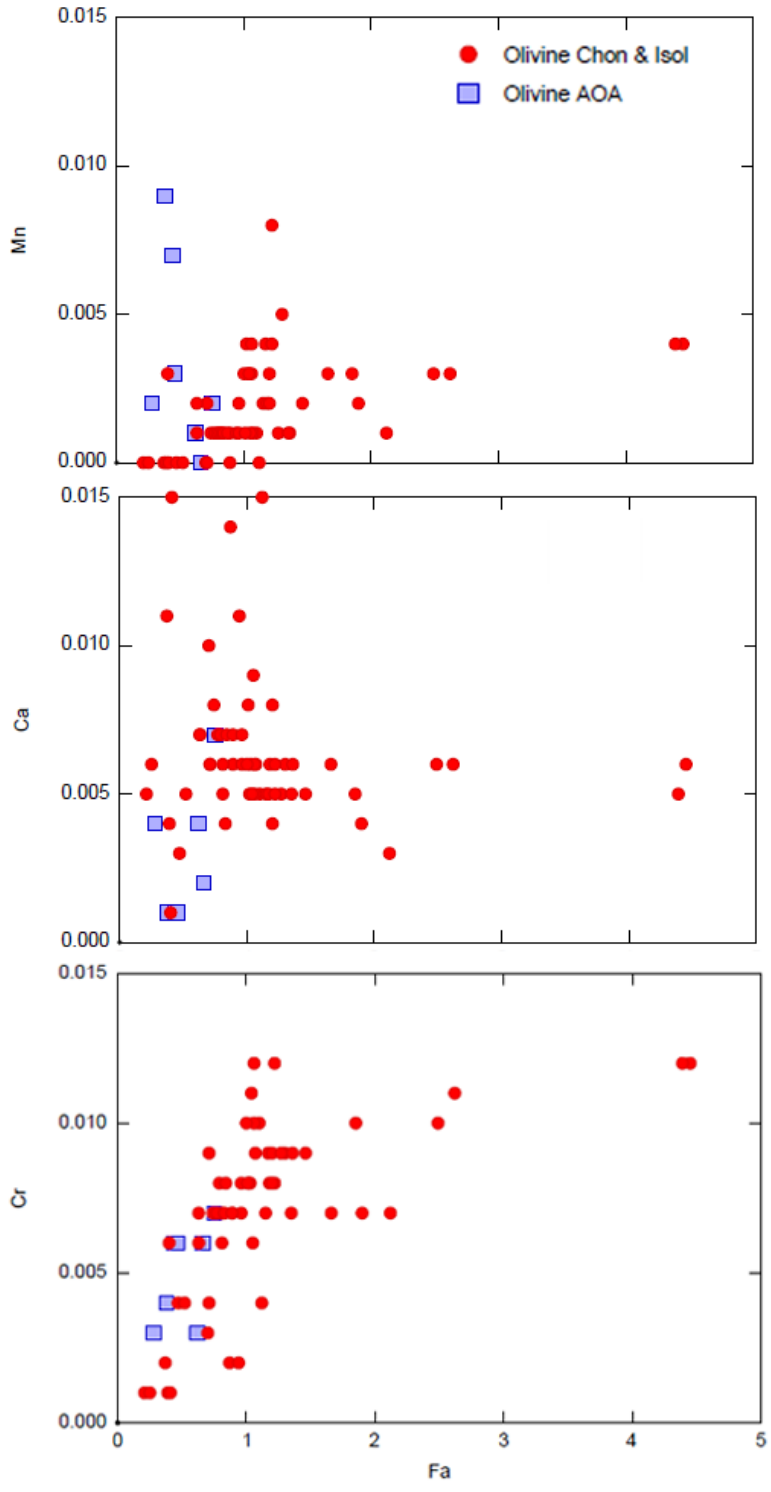

Fig. 5. Concentrations of Mn, Ca, and Cr in olivine in a.f.u. Olivine in AOA is closer to pure forsterite on average than that in chondrules (chon) and isolated (isol) in matrix.

3.2.2 Composite Al-rich chondrule

NWA 12563 contains one chondrule-like object (Fig. 6a) zoned with a core, a mantle with olivine and metal, and an igneous rim (in addition to the matrix-like fine-grained accretionary rim).We describe this chondrule as composite and Al-rich to call attention to the exceptional core that consists of a Ca- and Al-rich groundmass of plumose and acicular anorthite and diopside crystals (Fig. 6b). There are bladed and elongate hopper microphenocrysts of Ca-poor pyroxene, a magnesian pigeonite ($En_{90-94}Fs_{1-4}Wo_{4-7}$), occurring mainly in this core and the igneous rim. The mantle is discontinuous and resembles metal-rich microporphyritic Type IAm chondrule material with forsterite ($Fo_{99.1 \pm 0.2}$). Where the mantle is absent there are a few forsterite hopper crystals, as well as pigeonite set in the groundmass of the adjacent core. The igneous rim resembles Type IAB chondrules. Alteration is confined mainly to the rim and metal in the mantle, particularly in the continuous ring segment. A vug in the core contains amphibole growing inward, as well as some calcite whiskers (Fig. 6c). The Al-Ca-rich plumose core groundmass is similar to crystalline mesostasis in a Type I chondrule in CR3 chondrite QUE 99177 (Abreu and Brearley, 2010). Its texture is similar to those of rapidly cooled synthetic Al-rich chondrules (Tronche et al., 2007).

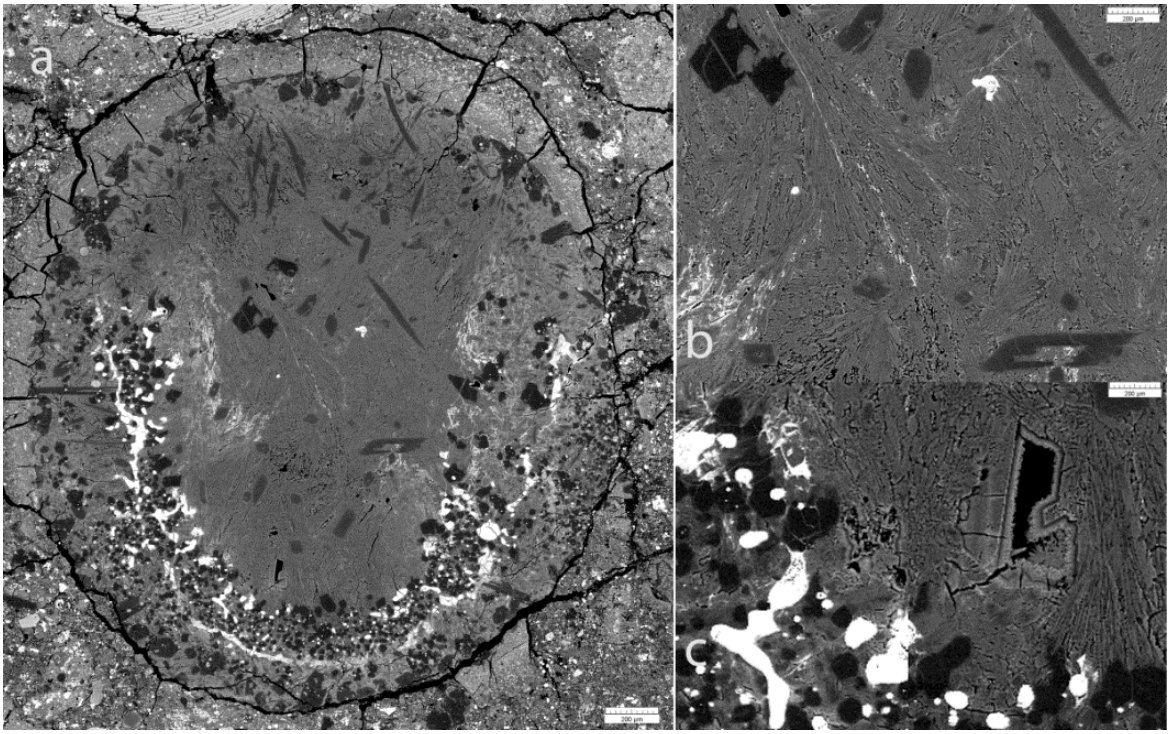

Fig. 6. BSE images of refractory chondrule. (a) Whole chondrule with core, mantle, igneous rim, and fine-grained rim. (b) Core of plumose anorthite and diopside crystals with elongate and hopper pigeonite microphenocrysts. (c) Amphibole-lined vug in core (center-right) and Type IAm chondrule mantle with unaltered metal (bottom left).

3.2.3 Chondrules

The chondrules are mainly Type IA (PO and BO) and IAB, including originally metal-rich chondrules, and Type IIA (PO and BO, with relict grains and minor chromite. They are illustrated in Fig. 7. Pyroxene-rich chondrule fragments are rare, and olivine is much more abundant than pyroxene in the

meteorite, as indicated by the histograms (Fig. 8a). Similarly, Type I chondrules and chondrule debris are more abundant (84%) than Type II material (16%).

Fig. 7. BSE images of chondrules. (a) Type IA porphyritic olivine chondrule with rare metal inside olivine. (b) Poikilitic Type IAB chondrule: ol olivine, op orthopyroxene, Di diopside, ps pseudomorph after metal. (c) Type IIA porphyritic olivine. (d) Type IIA barred olivine.

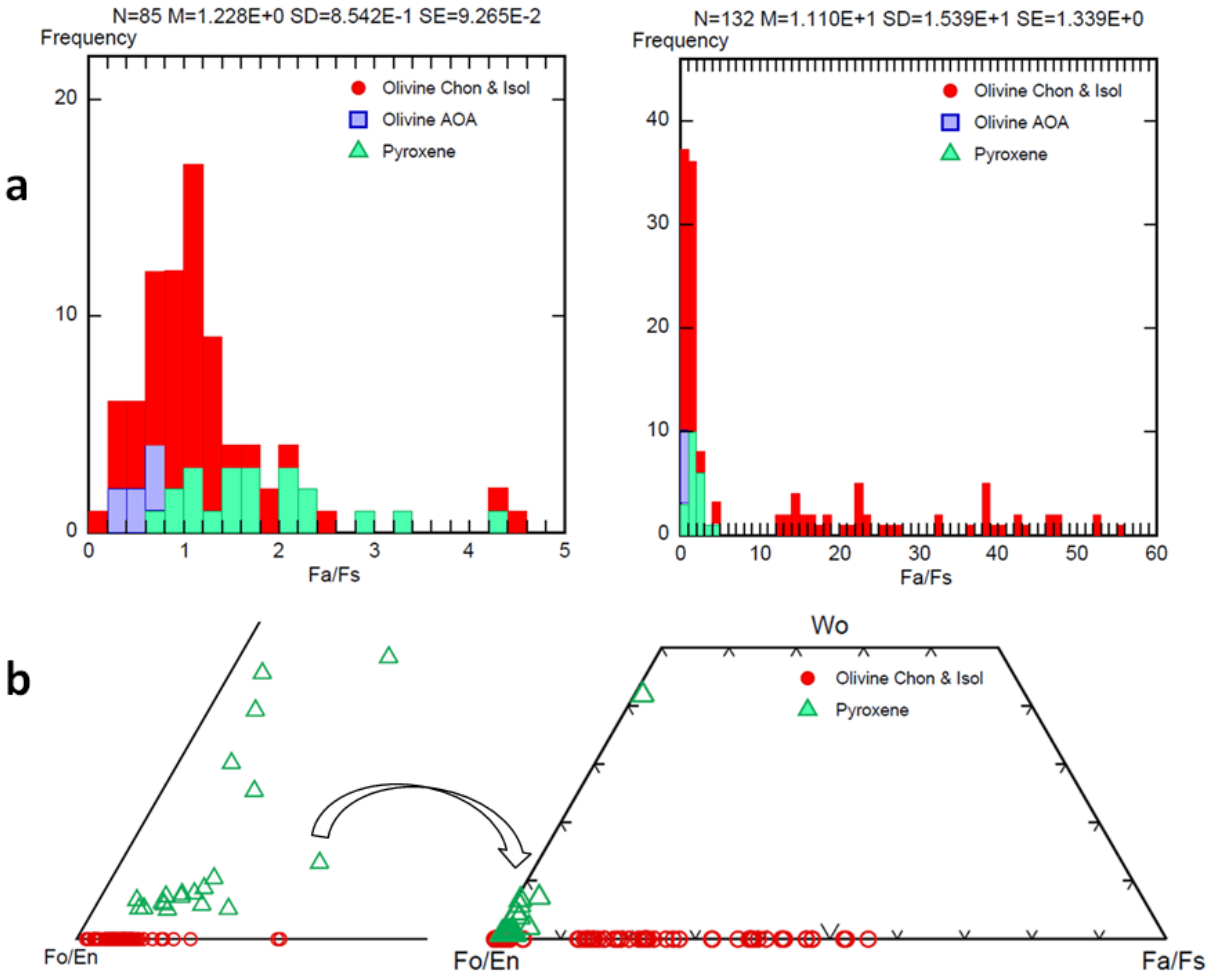

448

449

450 Fig. 8. (a) Histograms of olivine (in AOA and Types I and II chondrules) and pyroxene compositions. (b)
451 Olivine and pyroxene compositions. Detail of Type I olivine and pyroxene at left in both (a) and (b).

452 The forsteritic olivine of Type I chondrules has an average composition of $Fo_{98.9 \pm 0.7}$ with Fe correlating
453 with Cr and Mn (Fig. 5). Type IAB chondrule and isolated pyroxene in NWA 12563 are generally $En_{98-94}Fs_{1-4}Wo_{1-2}$ though there is minor interstitial diopside ($En_{57}Fs_1Wo_{42}$) in some chondrules (Fig. 7b). Type
455 II olivine has a composition range of Fo_{84-44} and an average FeO/MnO of 90, typical of carbonaceous
456 chondrites (Berlin et al., 2011; Hewins et al., 2014). The standard deviation of wt. % Cr_2O_3 in olivine is
457 lower than that in the CO 3.0 ALH 77307 (Fig. S2), placing it at 3.0 on the scale of Grossman and
458 Brearley (2005). Selected mineral compositions are given in Table 1.

3.3 Chondrule deformation and alteration

A few chondrules survive as complete objects with rims, but the majority are fragmented and/or deformed with many unusual shapes. In addition to hydrous replacement of many phases, especially glass (Fig.9a), many Type II barred olivine chondrules display fractures and kinking (Fig. S.3), and there is a kind of disbarring where olivine bar segments are scattered into adjacent matrix (Fig. 9b). Some Type I chondrules have highly irregular, gerrymandered shapes (Fig. 9c) in part caused by selective alteration of specific phases, probably metal, eating away at their borders. Similar embayments are observed in Tagish Lake (Takayama et al., 2012). Clusters of ferroan olivine crystals are interpreted as defunct Type II porphyritic chondrules that suffered replacement of mesostasis by a matrix-like assemblage with concentrations of phosphate (Fig. 9d).

Fig. 9. BSE images of chondrules. (a) Type IIA BO, with interstitial glass replaced by phyllosilicates. (b) Disbarred Type II BO, fragmented, kinked with bar fragments dispersed in matrix (center bottom). (c) Gerrymandered Type IA chondrule; embayments (e.g. dashed line) caused by replacement of least stable material. (d) A defunct Type IIA chondrule, with a cluster of phenocrysts and microphenocrysts in matrix-like altered mesostasis.

Though olivine in chondrules and matrix is essentially unaltered, pyroxene in chondrules shows incipient alteration. Kamacite and Ca-Al-rich glass survive only as rare inclusions in the forsterite of Type

I chondrules. The dominant chondrule alteration phases are fibrous to lathy Mg-Si-rich and Fe-Al-rich phyllosilicates visible in BSE as mixtures or intergrowths interstitial to microphenocrysts, i.e. replacing mesostasis (Fig. 10a,b). Pyroxene alteration in chondrules occurs along etched cleavage planes marked with voids and some phyllosilicate (Fig. 10c). Ovoid inclusions in olivine and particularly pyroxene on the margins of Type I chondrules (as shown in Fig. 10b,c,d,e). They have a form like that of large metal grains and we interpret them as pseudomorphs after kamacite, as in Wisconsin 9600 and Tagish Lake (Brearley, 2004; Takayama et al., 2012). There is a continuum (of smooth clear glassy-looking serpentine ovoids Fig. 10, particularly d), Si-poor ovoids speckled with high-Z material including sulfides, and manifestly altered, sometimes two-phase, Fe-rich nodules (Fig. 10f).

Fig. 10. BSE images of alteration in chondrules. (a) Type IA rich in altered metal and with phyllosilicates replacing mesostasis. (b) Metal-poor Type I chondrule with two-phase phyllosilicate (dark grey serpentine-saponite and light grey more ferroan chlorite). (c) Type IAB with fresh metal only in olivine at top left; phyllosilicates replace mesostasis and pseudomorph metal. (d) Metal pseudomorphs within pyroxene in a Type IAB chondrule composed of clear serpentine or serpentine speckled with FeNiCrPS phases. (e) Type IAB with phyllosilicate in etched pyroxene. (f) Type IA chondrule with

494 silicate contrast set to black; metal pseudomorphs are two-phase, Si-rich and S-rich respectively. Ol:
495 olivine, PX: pyroxene, PH: phyllosilicate, AK: altered kamacite, and psd: pseudomorph.

496 Analyses of alteration phases found in chondrules are given in Table 2. The two phases seen in
497 BSE images of mesostasis are called serpentine and chlorite here; altered metal ovoids consist of
498 assemblages of phyllosilicates and Fe-rich phases distinguished in Table 2 by the texture type. Some
499 analyses do not represent pure phases, as there may be inclusions of sulfides and other minerals, and
500 mixtures of phyllosilicates at the one micron scale. A secondary amorphous silicate phase does not seem
501 probable for the fibrous and lathy material in the chondrule mesostasis, but it cannot be ruled out for the
502 smooth ovoids.

503 Table 2. Analyses of alteration phases in mesostasis and ovoid inclusions replacing metal in chondrules.

Type	Sample	SiO2	Al2O3	TiO2	Cr2O3	FeO	MnO	MgO	CaO	Na2O	K2O	P2O5	S	Ni	Total
serpentine	134	45.02	2.74	0.09	0.43	11.86	0.17	27.73	0.04	0.46	0.06	0.02	0.31	0.06	88.99
	135	44.31	3.23	0.15	0.37	12.20	0.09	26.61	0.14	0.49	0.04	0.01	0.39	0.05	88.08
	42	44.27	3.85	0.07	1.43	12.03	0.04	25.27	0.33	0.79	0.25	0.03	0.16	0.11	88.64
	41	45.10	4.60	0.09	1.23	10.64	0.02	24.98	0.51	1.06	0.29	0.10	0.10	0.03	88.75
chlorite	17	40.63	8.12	0.21	1.01	15.91	0.13	23.59	0.30	0.84	0.16	0.07	0.25	bd	91.22
	26	37.90	9.54	0.32	0.90	14.28	0.08	24.83	0.12	0.60	0.14	0.23	0.24	0.03	89.21
	24	36.27	11.89	0.22	0.49	23.83	0.13	17.70	0.21	1.68	0.18	0.14	0.25	0.02	93.00
	20	31.96	17.08	0.27	0.40	18.58	0.27	20.13	1.63	0.69	0.09	0.51	0.33	0.02	91.96
ovoid (clear)	15	39.29	6.25	0.17	1.72	18.40	0.10	17.99	0.12	0.37	0.14	0.05	0.14	0.04	84.78
	14	36.84	6.50	0.42	3.14	19.54	0.20	17.07	0.16	0.19	0.11	0.11	0.29	0.04	84.60
	12	34.79	6.40	0.51	2.52	18.73	0.17	17.17	0.55	0.26	0.10	0.12	0.39	0.19	81.90
	33	29.46	5.30	0.10	4.30	20.46	0.08	14.73	1.20	0.08	0.07	0.28	0.42	1.25	77.73
ovoid (speckled)	32	29.37	3.54	0.29	5.86	34.58	0.08	6.76	2.20	0.22	0.13	0.49	1.54	2.88	87.94
	37	21.81	5.82	0.08	6.19	30.19	bd	11.35	1.31	0.26	0.13	0.44	1.80	2.18	81.56
	22	13.09	0.75	1.46	4.54	60.07	0.48	4.47	0.79	0.19	0.02	0.45	3.68	1.94	91.92
	36	10.10	0.78	1.49	3.68	51.70	0.38	3.37	1.47	0.17	0.07	0.83	5.06	3.37	82.47
ovoid (2-phase)	45/1	29.50	7.45	0.18	1.13	27.96	0.40	9.02	0.61	0.53	0.29	0.33	1.43	0.67	79.50
	36/1	2.81	0.08	0.03	1.67	81.37	0.29	0.52	0.22	0.11	bd	0.53	2.64	3.36	93.61
	47/1	5.71	1.60	0.05	0.42	53.68	0.03	3.20	0.23	0.11	0.03	0.25	15.88	10.31	91.50

504

505 Understanding of chondrite phyllosilicate compositions involves the roles of variations in
506 tetrahedral-octahedral layer combinations (serpentine vs. saponite, and interlayer cations), ionic
507 substitutions (especially Al), and the presence of inclusions (especially of sulfide) or mixed layer
508 structures. Charge balancing of Al in phyllosilicate is complex (Wiewora and Weiss, 1983) and here we
509 use the M_6Si_4 serpentine endmembers chrysotile-greenalite, where M = Mg, Fe^{2+}, and the M_5AlSi_3Al
510 chlorite midmembers clinochlore-chamosite to evaluate the identity of the phases. Analyses are plotted
511 along with serpentine, chlorite and saponite endmembers in Fig. 11. All the phyllosilicate analyses free of
512 obvious high-Z material plot between serpentine and saponite tie lines, with some analyses near the
513 chlorite tie line (Fig. 11a). A large range of Al contents is seen in Fig. 11b: most of the phyllosilicate
514 compositions (except ovoid pseudomorphs with high-Z inclusions) fall in a triangle bounded by
515 endmember serpentine, and mid-member chlorite and saponite compositions. Those with moderate Al

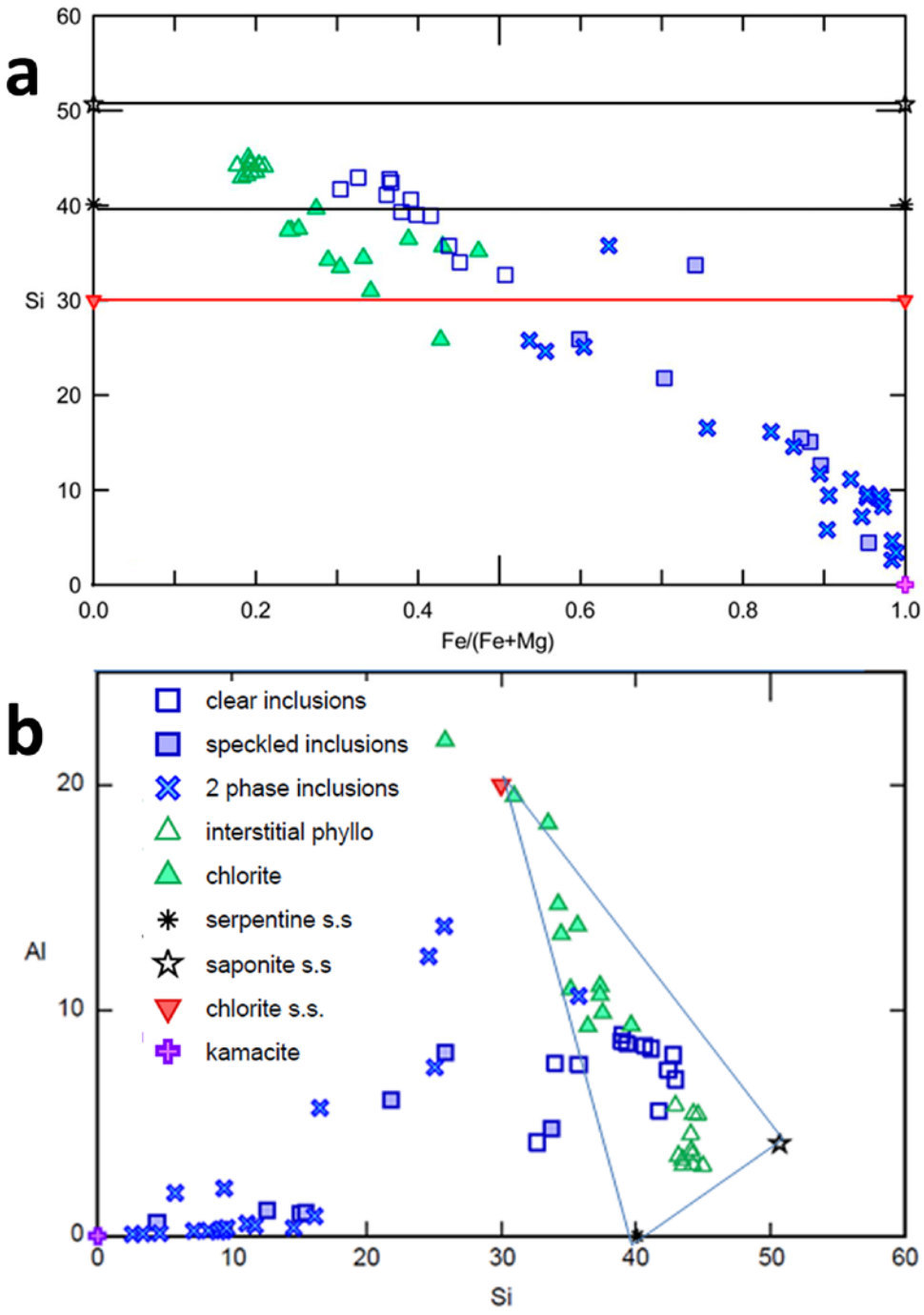

Fig. 11. Compositions of chondrule mesostasis (green) and metal alteration phases (blue) in atomic percent (excluding O) compared to reference s.s. (solid solution) serpentine, saponite, chlorite (clinochlore) and kamacite compositions. (a) Ovoid inclusion material ranges from compositions near kamacite to near chlorite and serpentine. (b) mesostasis phyllosilicates are magnesian serpentine-saponite mixtures or intergrowths and a ferroan chlorite. The distribution within the three-phase triangle suggests that chlorite is a mixture.

contents, with a maximum near clinochlore and a minimum near penninite (not shown), and with roughly equal quantities of ^{IV}Al and ^{VI}Al, are designated as chlorite. We cannot show that those with a composition near penninite are not mixtures of clinochlore-like chlorite and serpentine, or a mixed-layer phase, but compositions near clinochlore exist. The magnesian serpentine-like phyllosilicate is quite tightly clustered in composition (Fig. 11a,b open triangles) with some coupled Al substitution (Fig 11c) as in chlorite. However, chlorite is more ferroan than the serpentine-saponite and has a wide range of Fe/Mg ratios (Fig. 11a). The correlation of Fe/Mg is positive with Al and negative with Si, for both interstitial chlorite and ovoid inclusions. The phyllosilicate with lower Al contents falls close to a tie line between Mg-rich serpentine and saponite (Fig. 11b). In general, it has an octahedral to tetrahedral cation ratio between 3:2 and 3:4, corresponding on average to serpentine with about 45% saponite.

There is a continuum of compositions for two-phase, speckled, and clear ovoid inclusions (Fig. 10 f, d, c, respectively) between metal and phyllosilicate replacing mesostasis, particularly chlorite (Fig. 11, 12). Fe and Ni concentrations are naturally lower in the silicate inclusions than in reference kamacite, but P, S and Cr are higher, especially in the ovoids speckled with inclusions. Clear ovoids are close in composition to chlorite, except for higher Cr, lower Al (Fig. 11, 12) and lower P. The least altered ovoids appear in BSE to be two-phase mixtures (Fig. 10f). These ‘phases’ are dominantly Si-rich (phyllosilicate) and dominantly Fe- or S-rich, i.e. in reality three-component mixes. The Fe-rich phase could be residual kamacite, magnetite or a hydroxide; the S-rich component is one or more sulfides, as tochilinite (Tomeoka and Buseck, 1985) is eliminated by the low Mg content of the replacing high-Z phases (Fig. 11a). The “two-phase” pseudomorphs have Ni, Cr and P contents higher than those of the speckled inclusions.

Fig. 12. Minor element concentrations of ovoid inclusions pseudomorphing metal in atomic percent (excluding O) compared to mesostasis phyllosilicates and a reference kamacite composition. Concentrations of S, Cr, and P are higher than for kamacite, even for clear ovoids whose composition is close to chlorite for major elements.

3.4 Matrix and rims, mineralogy and alteration

3.4.1 Overview of matrix

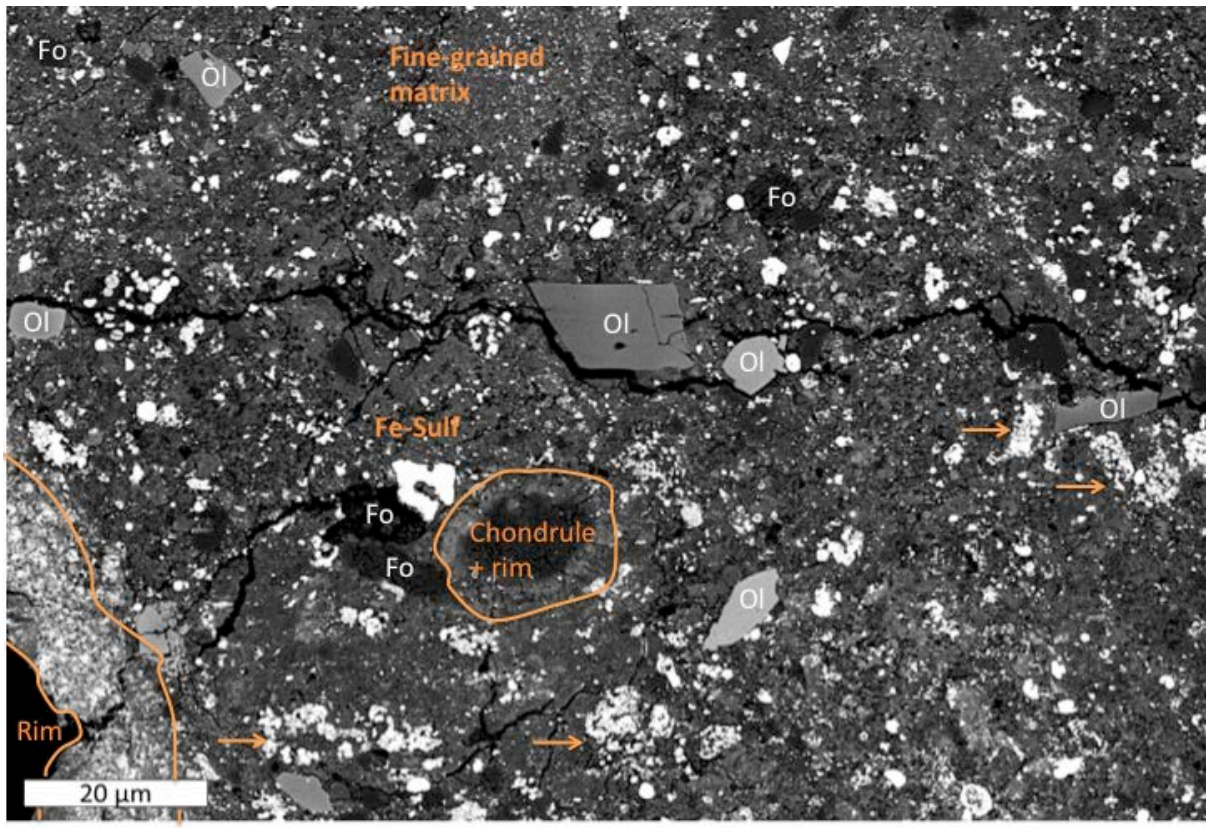

Fig. 13. BSE image of a representative area of the matrix of NWA 12563. The different minerals are Ol (olivine with various Fe contents), Fo (forsterite), and Fe-sulf (Fe-rich sulfide). The orange arrows indicate the presence of framboidal magnetite aggregates.

A general view of the matrix of NWA 12563 is shown in Fig. 13. The grain size ranges from <100 nm to 20 µm, but some grains are larger, such as patches of carbonate, and type I and type II chondrule fragments. The type I chondrule fragments are mainly pure forsterite which sometimes contain preserved metal grains as inclusions. The type II fragments have sharp outlines and generally show Mg/Fe zonation in olivine with a more Mg-rich core. The pyroxene grains are anhedral, as in the chondrules, and show chemical zonation, from a stoichiometric pyroxene in the center of the grain to more oxygen-rich towards the edges. EPMA data do not reveal the presence of the tochilinite-cronstedtite intergrowths usually observed in CMs and other altered carbonaceous chondrites.

A striking feature of the matrix is the occurrence of sulfides and magnetite: both occur as small grains, embedded within the amorphous silicates/phyllosilicate, and also as scattered rosette-like aggregates. The particle size of the matrix-embedded magnetite is very well constrained since it varies between 100 nm and a few µm, with rare grains 10-20 µm in size. Magnetite mainly occurs as framboidal and spheroidal aggregates, but also as plaquettes (Fig. 14a). Its composition is Fe_3O_4 and no other elements are present above the detection limits. There is also magnetite occurring as a fine meshwork within the sulfide rosettes (Fig. 14c,d). A bulk magnetite content of 6.80 wt. % was estimated based on the magnetic properties. This translates into 2.94 vol% assuming a CM2 bulk density of 2.25 for NWA 12653 (Consolmagno et al., 2008).

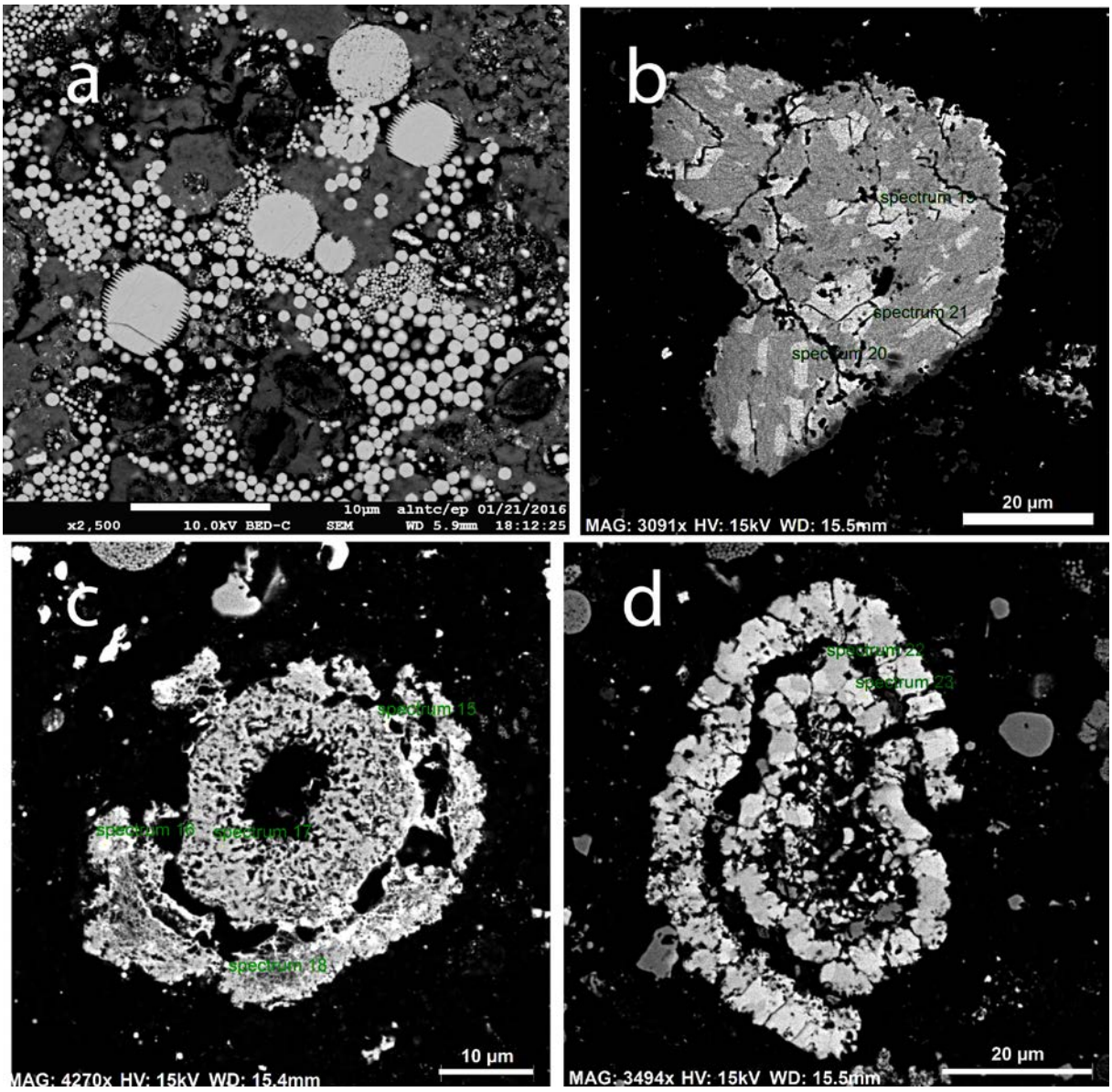

Fig. 14. BSE images of fine-grained magnetite and sulfide in matrix. (a) Framboidal and plaquette magnetite. (b) Troilite with exsolved pentlandite. (c,d) Rosette aggregates of pentlandite, troilite and magnetite.

Pentlandite is the main sulfide mineral in the matrix, occurring as isolated or clustered tiny laths, as rosettes, and rarely as exsolution lamellae within troilite (Fig. 14b). The rosette or flower structures are mainly double rings. They contain pentlandite, troilite and magnetite (Fig. 15c,d). Pentlandite compositions plot on the linear field for pentlandite in the 200°C section of the Fe-Ni- S system, reconstructed using reference compositions from Craig (1973) and Harries and Langenhorst (2013). Their most Fe-rich compositions are in equilibrium with the pyrrhotite near stoichiometric troilite (Fig. S4). Magnetite occurs in a fine meshwork with sulfide (Fig. 14c), the lacey texture suggesting replacement of either phase by the other.

3.4.2 Matrix mineralogy using ACADEMY

We used the ACADEMY method (Zanetta et al., 2019) to characterize matrix. This method allows us to establish phase maps as well as modal abundances using low voltage SEM and then to quantify the mapped area using EPMA.

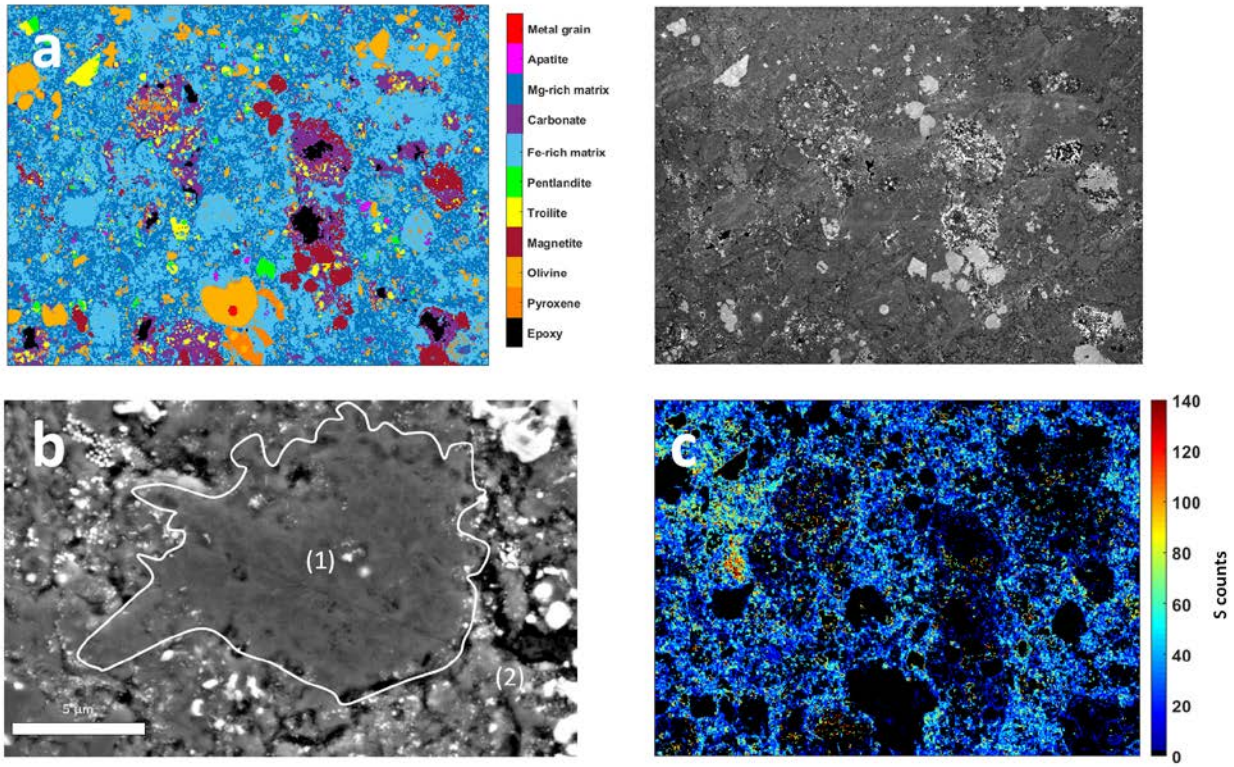

Fig. 15. (a) Phase map (125 µm*96 µm, pixel size ~ 250 nm) obtained using the ACADEMY methodology (Zanetta et al., 2019) and corresponding secondary electron image. It reveals in particular two types of fine-grained matrix material (different blues) with different texture and composition. (b) High resolution BSE image of these two types of fine-grained material. (1) is a homogeneous and fibrous phyllosilicate and contains few inclusions. (2) contains amorphous silicate richer in nanosulfides and is more porous. (c) X-ray map showing the localization of S-rich matrix near some sulfide grains seen in (a).

The phase map (Fig. 15a) reveals that the matrix of NWA 12563 is dominated by a groundmass of amorphous silicate and phyllosilicate. Sulfides, oxides, anhydrous silicates and carbonates are embedded in this groundmass. The bulk composition of this area is near-chondritic (Table 3), with the exception of calcium which is enriched due to the presence of large dolomite grains. The abundance of magnetite is

around 4 % in this area (Table 3) and reaches up to 10 % in other areas of the meteorite. Framboidal magnetite is associated with Mg-rich carbonate. The amorphous silicate/phyllosilicate is seen on the BSE map to be divided into two sub-types (Fig. 15b). The first one (1) displays a fibrous texture and is richer in Mg (i.e. Mg-rich matrix). The second one (2) contains a higher content of nanosulfides which are below the mapping resolution and thus it appears richer in Fe (Fe-rich matrix). It is also more porous. In a few locations enrichment in S was visible in the amorphous/phyllosilicate material around the nanosulfides (Fig 15c). We classified these areas containing fine troilite and pentlandite as S-rich matrix.

Table 3. Area abundances of matrix phases from ~1 mm^2 phase map.

Mg-rich matrix	33.94%
Fe-rich matrix	30.18%
S-rich matrix	10.66%
Si-rich matrix	1.55%
Olivine	4.09%
Metal grain	0.04%
Pyroxene	4.18%
Magnetite	4.06%
Carbonate	8.02%
Troilite	2.29%
Pentlandite	0.79%
Apatite	0.19%

3.4.3 TEM analysis of matrix and chondrule rims

We studied several FIB sections which all present relatively homogeneous crystalline fibrous phyllosilicates next to more heterogeneous areas containing amorphous silicate and nanosulfides, oxides and organics. The finer scale TEM map showed very similar matrix details to those made by SEM (Fig. 15b). We observed wide fields of relatively homogeneous fibrous phyllosilicates, juxtaposed with more heterogeneous areas rich in amorphous silicate and nanosulfides (Fig. 16). Sulfides occur principally as nano-cristalline aggregates and scattered needles. An Mg-Fe-Ni-Ca-S x-ray map of the same area is shown in Fig. S5.

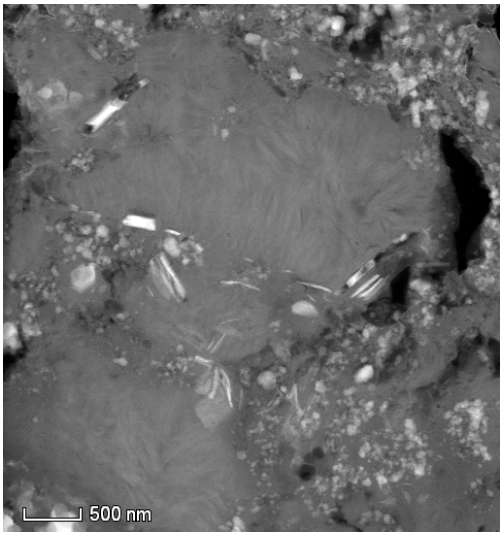

Fig. 16. STEM Bright-field (BF) image of a typical area of the matrix of NWA 12563, showing phyllosilicate-rich patches and multi-phase regions with amorphous silicate and sulfide inclusions.

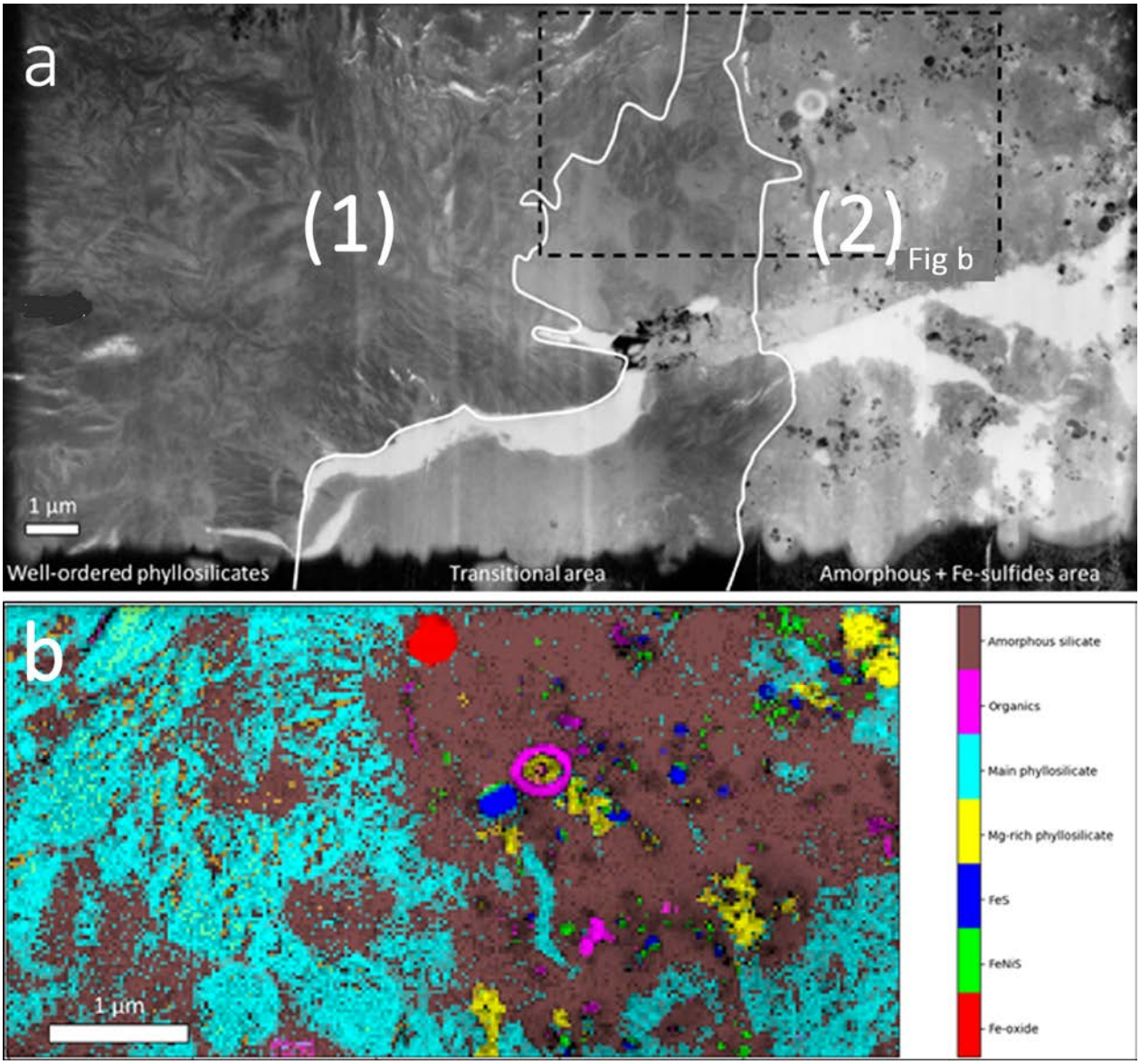

Fig 17. (a) STEM Bright-field (BF) image of a typical area of the matrix of the NWA 12563 chondrite, showing (1) phyllosilicate-rich patches and (2) heterogenenous regions dominated by amorphous silicates. The box outlined is shown in (b) a phase map of sulfide-poor fibrous phyllosilicate regions (1) and their transition to sulfide-rich amorphous regions.

Phyllosilicate fibers are ~500 nm long in Fig. 15b and 16, but well ordered fibers ~1 µm long are seen in Fig. 17a, where there are transitional regions between phllosilicate patches and amorphous silicate patches. We quantified the compositions of phyllosilicate and amorphous silicate at each pixel across the three regions seen in Fig. 17 (Table 4 and S3). The aluminum content of matrix phyllosilicate, unlike that for chondrules, is too low to be compatible with chlorite. The phyllosilicate has the same composition throughout, with an (Mg+Fe)/Si ratio of 1.16, intermediate between the ratios of saponite and serpentine, as in chondrule mesostasis but more ferroan (Fig. 18). Amorphous silicate displays an (Mg+Fe)/Si ratio of 0.97 in region (2) and 1.05 in the transitional region, with much less Fe than in CR and CM chondrites (Chizmadia and Brearley, 2008; Abreu and Brearley, 2010; Le Guillou et al., 2015; Vinogradoff et al.,

2018). The Fe/Si ratio is fairly constant (~20.30) through the three regions, including intermediate areas, but the concentration of S and Ni differs. Iron-rich analyses in Fig. 18b are also Ni- and S-rich, reflecting numerous nanosulfide grains in the amorphous silicate. The heterogeneous distribution of sulfide grains in amorphous silicate is seen In Table 4, where the standard deviations for S and Ni are much higher than the mean values. The Fe-rich sulfide is pyrrhotite based on the (Fe+Ni)/S ratio of the most S-rich analyses, and consists of 100-200 nm grains. It is surrounded by smaller grains of the less abundant pentlandite. Organic particles, clusters of anhydrous silicates, and one magnetite grain (~ 400 nm) are also observed in Fig. 17b but in low abundances. However, C and N are present in all analyses of amorphous silicate and pyllosilicate, with similar abundances and C/N ratios (Table 4). We corrected the compositions for the presence of organics and sulfide, and calculated a structural formula for the phyllosilicate, assuming 3 octahedral cations per formula unit. The average analysis of the amorphous silicate is presented in the same format for comparison purposes.

Table 4. Average compositions (ATEM) of matrix amorphous silicate (ams) and phyllosilicate (phyllo) in atomic % and atoms per formula unit.

Atom %	ave ams	s.d.	ave phyllo	s.d.	ams SIL	phyllo SIL	ams afu	phyllo afu
Si	13.21	0.87	14.63	0.69	15.47	16.42	2.97	2.58
Al	1.02	0.16	1.35	0.24	1.19	1.52	0.23	0.24
Ti	0.017	0.007	0.006	0.004	0.020	0.010	0.000	0.000
Cr	0.114	0.018	0.129	0.022	0.130	0.140	0.030	0.020
Fe	4.56	1.02	4.72	0.50	5.34	5.30	1.03	0.83
Mn	0.000	0.000	0.000	0.000	0.000	0.000	0.000	0.000
Mg	8.78	1.26	12.26	1.06	10.28	13.76	1.97	2.17
Ca	0.33	0.12	0.09	0.05	0.39	0.10	0.07	0.02
Na	0.28	0.06	0.53	0.07	0.33	0.59	0.06	0.09
K	0.029	0.007	0.013	0.006	0.030	0.010	0.010	0.000
P	0.001	0.002	0.000	0.001	0.000	0.000	0.000	0.000
S	0.97	1.43	0.14	0.11				
Ni	0.111	0.271	0.007	0.009				
Cl	0.063	0.059	0.050	0.023	0.070	0.060	0.010	0.010
C	12.42	2.39	9.90	1.95				
N	1.12	0.30	0.82	0.24				
O	56.97	2.32	55.34	1.34	66.74	62.09	12.81	9.77
Total	100.00		100.00		100.00	100.00	100.00	100.00

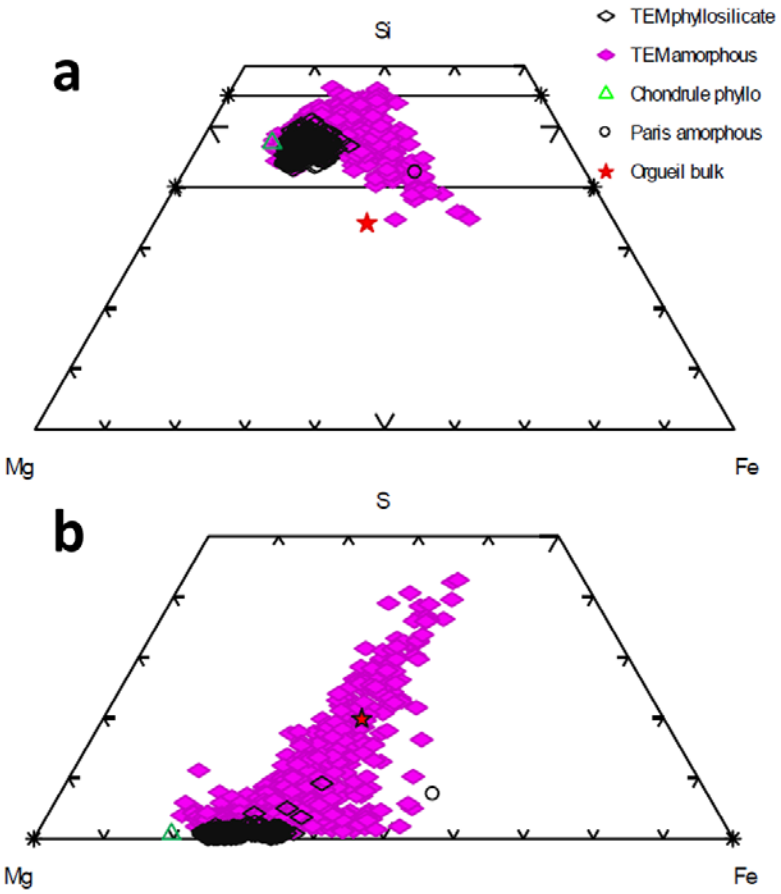

Fig.18. Compositions in atom % determined by ATEM (a) Mg-SiAl-Fe diagram showing that the phyllosilicate and amorphous silicate compositions are intermediate between saponite and serpentine stoichiometry (tie lines for reference). The phyllosilicate has a narrower range of composition and generally plots on the Mg-rich end of the compositional range. (b) Mg-S-Fe diagram showing that the more Fe-rich points of the amorphous silicates are due to mixture with Fe-Ni nanosulfides. Orgueil composition from Jarosewich (1990); Paris amorphous silicate from Hewins et al. (2014).

3.4.4 Fine-grained rims

Many chondrules in NWA 12563 are surrounded by accretionary rims that are bright in BSE because of very fine Fe-rich grains, and discrete clusters of fine magnetite spherules (Fig. 1, 6, 10, 14). The large composite Al-rich and relatively metal-poor chondrule of Fig. 6 has a rim with little obvious magnetite. Similarly, AOA and Type II chondrules do not have bright rims. Some, especially Type IAB chondrules have a halo of altered chondrule material with pseudomorphs after metal beneath the fine-grained rim. The sporadic nature of rim occurrence suggests a regolith history but a detailed study of fine-grained rims suggests that chondrules in Semarkona suggests rimming and fracturing of chondrules in the disk before accretion together with matrix dust (Zanetta et al., 2021).

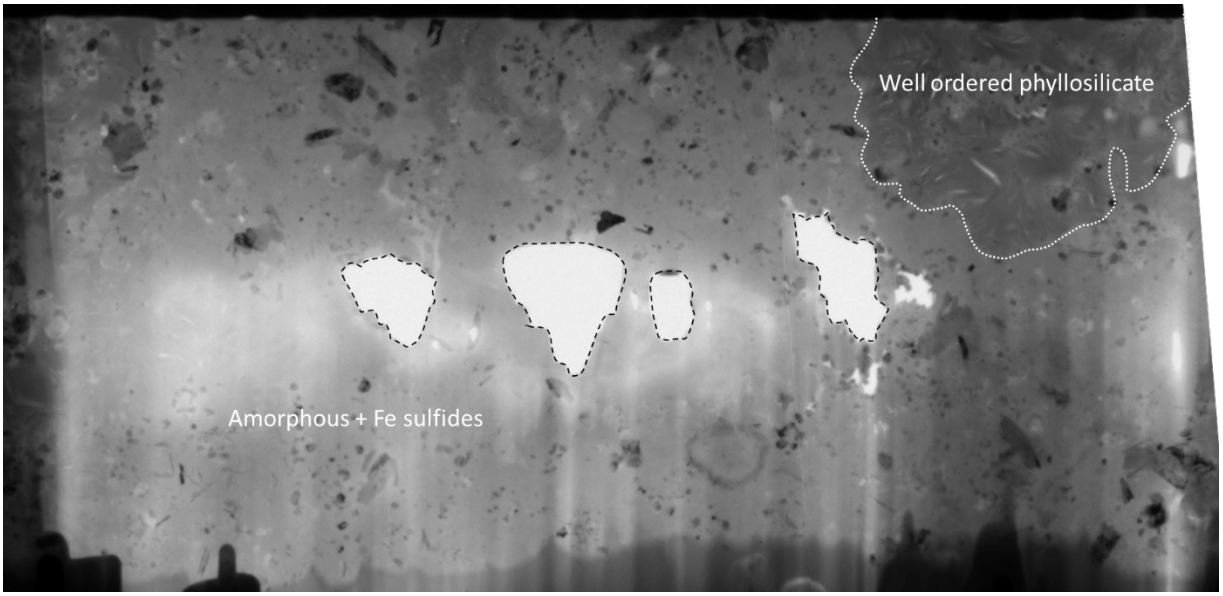

Fig. 19. STEM BF image of the FIB section ~20 µm long sampled in a fine-grained rim with amorphous silicate (light grey) locally with fibrous phyllosilicate crystals, organic material and anhydrous silicate (medium grey), pores (black) and holes (white).

An FIB section has been sampled in one of those fine-grained rims (Fig. 19). This rim consists mostly of amorphous silicates with embedded nanosulfides, small anhydrous silicate grains (<1µm) and organic matter. Rare patches of ordered phyllosilicates are visible. The rim differs from the amorphous patches in matrix in that the porosity is much lower. The large holes in the middle of the section are due to FIB damage during the final thinning operation. The compositions of the amorphous silicates and phyllosilicate patches are comparable to those of the matrix.

3.4.5 Iron valency in matrix material

The iron valency of amorphous silicate and phyllosilicate was measured by STXM on an FIB section that had not been previously observed by TEM. The spatial resolution is not sufficient to allow us to always distinguish between amorphous silicate and phyllosilicate, and some pixels might contain a mixture of both. Using the calibration proposed by Le Guillou et al. (2015), we quantified the $Fe^{3+}/\sum Fe$ ratio and obtained a value of ~ 75 % (±5), a value similar to that found in most CR chondrites (Le Guillou et al., 2015), in Acfer 094 (Hopp and Volmer, 2018) and in Semarkona (Dobrica et al., 2019).

3.4.6 The nature of organic matter

We studied individual organic particles, diffuse organics trapped within amorphous/phyllosilicates and carbonate grains by STXM on a FIB section. XANES spectra of the organic matter at the carbon K-edge were obtained. The main functional groups observed are: aromatic-olefinic at 285 eV, ketone-phenol at 286.5 eV, aliphatic at 287.5 eV, carboxylic acid at 288.6 eV and carbonate at 291.3 eV. The color map (Fig. 20) represents the three different components that we identified: individual organic particles (red), diffuse organics trapped within amorphous/phyllosilicates (green) and (~ 500 nm) carbonate grains. We found individual organic particles slightly more aromatic-olefinic rich than the surrounding diffuse organic

matter (dark red), associated with amorphous silicate and/or phyllosilicates, that is richer in aliphatics and carboxylic functional groups.

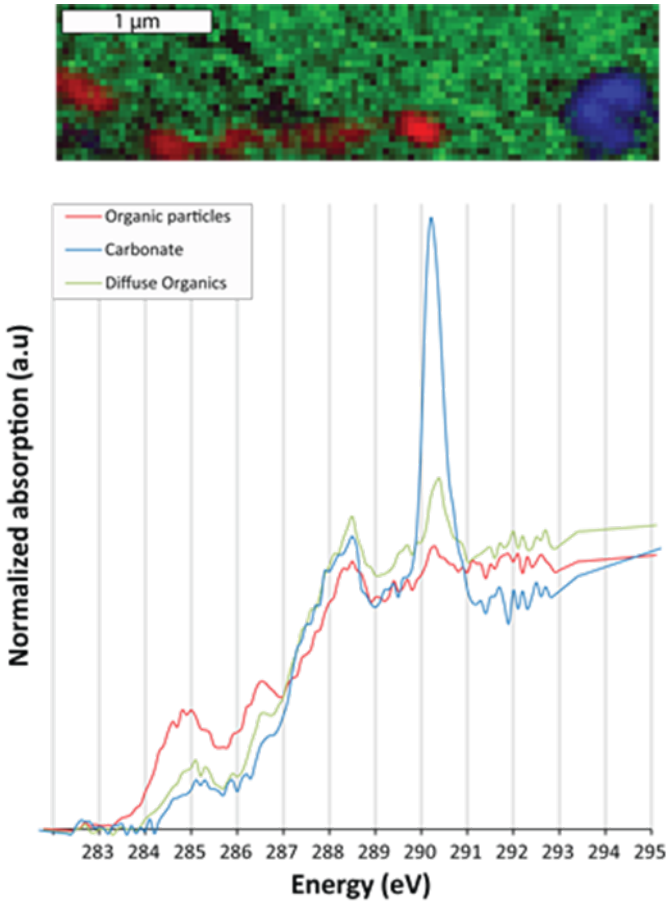

Fig. 20. XANES spectra at the carbon K edge obtained on a matrix FIB section. The color map shows individual organic particles, diffuse organics trapped within amorphous/phyllosilicates and carbonate grains.

We acquired Raman spectra on an epoxy-free section and compared them in Fig. 21 to the spectra of the insoluble organic matter of Murchison and Paris CM chondrites (Vinogradoff et al., 2018). The D band of NWA 12563 spectra is slightly more intense. However, NWA 12536 spectra were measured on meteorite chips and therefore include the contribution of the soluble organic compounds, whereas this is not the case for the Murchison and Paris spectra, and could explain the difference. They are also similar to published data for CM2 chondrites (Bonal et al., 2006, 2007; Busemann et al., 2007; Quirico et al., 2018). Therefore, the subtle differences between them cannot be clearly interpreted. The main result is that no significant difference is observed, and that, within a few tens of degrees, the peak temperature encountered by organics was similar to that of CM2 chondrites, i.e. below 250°C (Busemann et al., 2007).

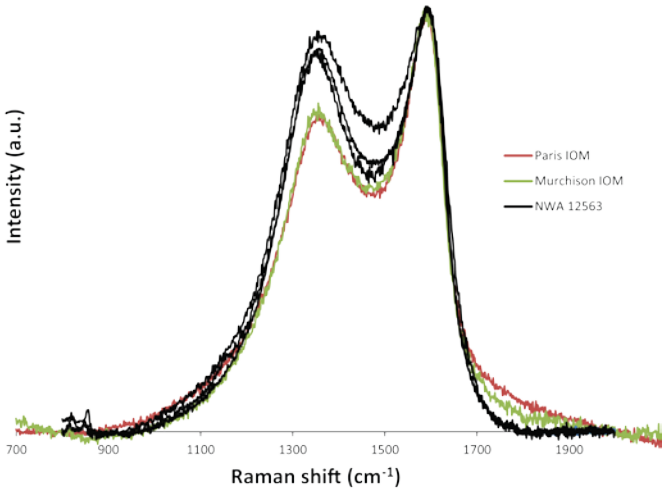

Fig. 21. Raman spectra of the NWA 12563 chondrite compared to spectra from CM2 chondrites.

3.4.7 Spectral properties

The large scale (mm-sized spot) diffuse Vis-NIR and confocal MIR reflectance spectra of NWA 12563 are reported in Fig. 22. The reflectance in the visible at 0.55 µm is found to be R=6.2±0.5%, while the spectral slope in the 0.45-1.0 µm range is slope = 0.27±0.07 µm^{-1}. In both cases, uncertainties represent a 1 sigma error bar. The left shoulder of a 1-µm band typical of olivine can be seen in the spectrum. Other features are an inflection between 0.6 and 0.7 µm, and a dramatic drop in reflectance for wavelengths below 0.59 µm. At much smaller spatial scale (less than 50 µm), the meteorite show very heterogeneous values of both albedo and spectral slope. The reflectance at 0.55 µm can be as low as R=3.9±0.7% in dark matrix areas, whereas it rises up to about R=24.6±0.7% in bright magnetite-rich areas. The corresponding spectral slopes vary from very "red" in dark matrix areas (0.39±0.1 µm^{-1}) to very "blue" in magnetite-rich areas (-0.54±0.02 µm^{-1}). A potential weak hydration feature around 0.64 µm is detected in some matrix locations.

The average MIR spectrum of NWA 12563 (Fig. 22b) shows a clear transition between the volume scattering regime and the surface scattering regime around 1150 cm-1 (~8.7 µm, main Christiansen feature). Bands at higher wavenumbers (lower wavelengths) are detected as absorption features towards the bottom. These include a weak hydration feature at 3700 cm^{-1} (2.7 µm), typical of phyllosilicates, and an extremely weak aliphatic CH feature around 2900-3000 cm^{-1} (3.4 µm). Overall, the OH and CH features in the volume scattering spectral range appear relatively weak, especially with respect to features at longer wavelengths, and this is probably due to the geometry of our measurements (backscattering) which tends to favor the surface scattering rather than the volume scattering regime. However, this observation is consistent with the H content observed, which is low compared to average CM2 chondrites. For wavenumbers lower (wavelengths higher) than the position of the main Christiansen feature, strong reststrahlen bands are observed as peaks towards the top, such as the peaks at 985 cm^{-1} (10.15 µm) and at 874 cm^{-1} (11.44 µm), that are generally attributed to hydrated silicates and olivine respectively. Smaller features between 945-960 cm^{-1} (10.4-10.6 µm) may be attributed to pyroxenes and other anhydrous phases. A small spectral contribution from carbonates is probably observed between 1410-1470 cm^{-1} (6.8-7.1 µm). Minor bands are present around 765-785 cm^{-1} (12.7-13.1 µm), which might be related to different types of oxides.

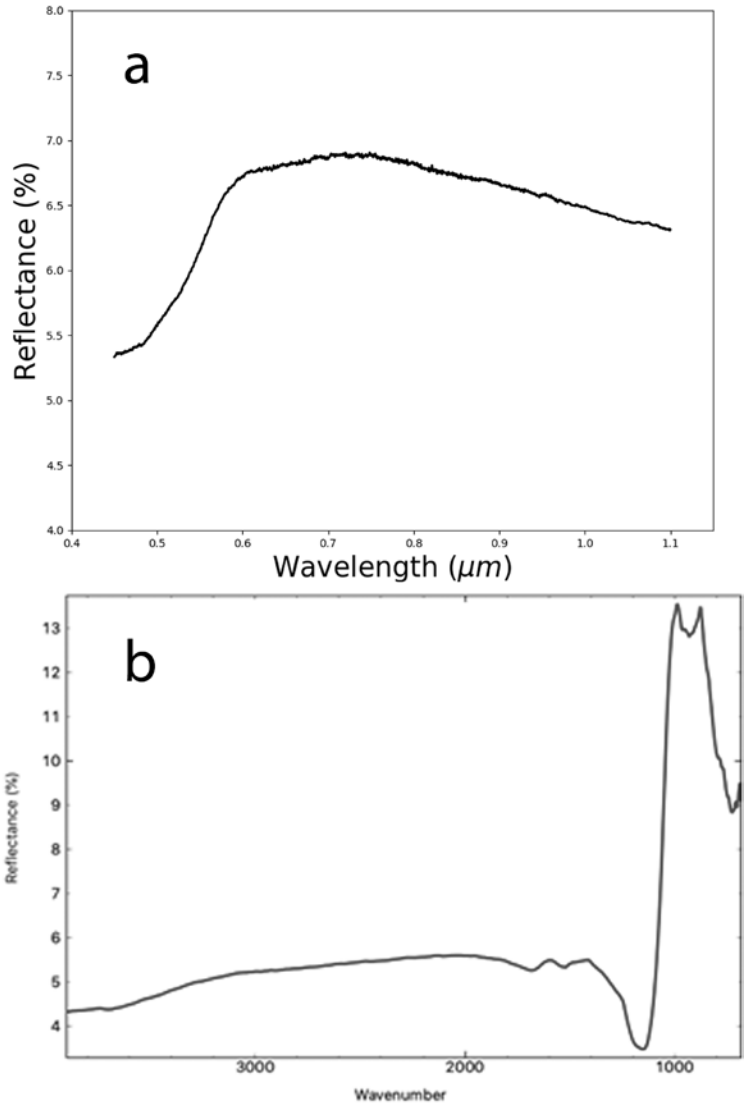

738

739 Fig. 22. Diffuse Vis-NIR (a) and confocal MIR reflectance spectra (b) of a chip of NWA 12563. (a) shows
740 the left shoulder of a 1-μm band typical of olivines. (b) shows a weak hydration feature at 3700 cm^{-1} (2.7
741 μm), typical of phyllosilicates, and an extremely weak aliphatic CH feature around 2900-3000 cm^{-1} (3.4
742 μm), and peaks at 985 cm^{-1} (10.15 μm) and 874 cm^{-1} (11.44 μm), due to hydrated silicates and olivine
743 respectively.

744 The presence of magnetite is not obvious in spectra measured on large surface areas of NWA
745 12563, e.g. a 400 mm matrix region in Fig. 23. However, the spectrum for the center of this area
746 containing a clump of framboidal magnetite shows the 564 cm^{-1} (17.7 μm) band for magnetite seen at 555
747 cm^{-1} in Bennu (Hamilton et al., 2019).

748

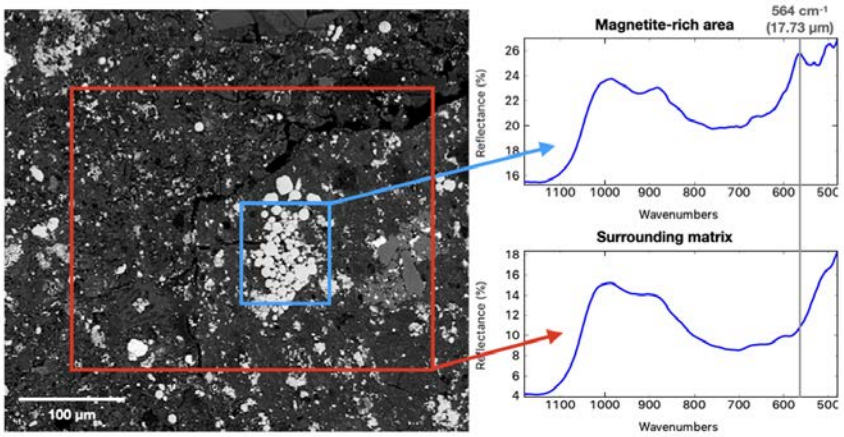

Fig. 23. The MIR spectral signature of magnetite at 564 cm^{-1} (17.73 μm) is observed from a small body of framboids but is obscured when a small region of matrix is analyzed.

4. DISCUSSION

4.1 NWA 12563 is unlike CM2 chondrites

Though the abundances of anhydrous silicates, matrix and phyllosilicates suggest that NWA 12563 is a C2 chondrite, considering secondary minerals, it is not immediately clear what class it represents. Although the matrix is more abundant than in most CM2 chondrites, relatively little of its amorphous silicate is converted to phyllosilicate. We examine several key properties and alteration mineral assemblages in NWA 12563 in Table 5. Its O isotope composition is at the $\delta^{18}O$-rich end of the CM range and close to Bells and Essebi (Fig. 2). The C and N abundances, and H isotopic composition for NWA 12563 are typical of CM chondrites (Pearson et al., 2006; Alexander et al., 2010, 2013. Vacher et al., 2020) but not that far from those of CY (heated) chondrites (Table 5). The $\delta^{13}C$ is considerably lower than in CM chondrites and similar to that in CI chondrites.

From Acfer 094 (Bischoff and Geiger, 1994; Newton et al., 1995; Greshake, 1997), Asuka 12169 (M. Kimura et al., 2019; Noguchi et al., 2020), DOM 08006 (Alexander et al., 2018; Nittler et al., 2018; Davidson et al., 2019) and MET 00426 and QUE 99177 (Abreu and Brearley, 2010; Le Guillou and Brearley, 2014; Harju et al., 2014; McAdam et al., 2018), among the most pristine carbonaceous chondrites, we can infer that the main primary phases in chondrules and matrix in 3.0 carbonaceous chondrites are olivine, pyroxene, glass, kamacite, sulfide (including nanosulfide <100 nm) and amorphous silicate. The transformation of these phases, along with ice and organic material, has led to different suites of secondary phases in C2 chondrites.

Aqueous alteration of olivine mainly produces serpentine, and carbonaceous chondrite matrices contain serpentine minerals, yet olivine phenocrysts in chondrules do not disappear until the CM2.0/2.1 alteration stage e.g. LAP 02277 (Hanowski and Brearley, 2001; Rubin et al., 2007). Though alteration of olivine can be used to designate subgroups (Hanowski and Brearley, 2001; Velbel et al., 2015), many other primary phases are more useful in subdividing CM2 chondrites: kamacite, matrix amorphous silicate, and chondrule glass are replaced before olivine is much affected. Approaches tracking single facets of alteration, e.g. replacement of kamacite (M. Kimura et al., 2011; Palmer and Lauretta, 2011), hydrogen abundance (Alexander, 2013), or total phyllosilicate abundance (Howard et al., 2015), are useful individually but are difficult to combine in a consistent manner. Holistic approaches (e.g. Rubin et al., 2007; Velbel et al., 2015) have been used successfully with moderately to totally altered CM chondrites, where key steps are the development of cronstedtite and tochilinite and their eventual disappearance.

The chondrule kamacite in NWA 12563 is pseudomorphed by serpentine with no tochilinite, whereas in CM2 chondrites the metal is replaced by tochilinite and cronstedtite (Tomeoka and Buseck, 1985; McSween, 1987; Rubin et al., 2007; Maeda et al., 2009; Palmer and Lauretta, 2011; Vacher et al., 2019). The occurrence of tochilinite is almost confined to CM2 chondrites (Zolensky et al., 1993; Rubin et al., 2007; Pignatelli et al., 2017) and its abundance is much lower in CM1. CM1 chondrites differ from NWA 12563, in having less olivine, less magnetite, less amorphous silicate, and more phyllosilicate (King et al., 2017). For other chondrite groups, minor amounts have been observed only in CR chondrites (Le Guillou and Brearley, 2014; Changela et al., 2018) though other aspects of their alteration are similar to those of CM chondrites (Harju et al., 2014). We have not observed tochilinite in NWA 12563. Its chondrule mesostasis contains amorphous silicate, serpentine-saponite, and chlorite rather than serpentine and cronstedtite, as in CM2 chondrites. Its matrix contains abundant amorphous silicate, serpentine-saponite, and magnetite, whereas CM2 matrix contains amorphous silicate in the least altered samples (Hewins et al., 2014), serpentine, cronstedtite, and tochilinite (Ikeda, 1983; Zolensky et al., 1993; Rubin et al., 2007; Velbel et al., 2015; Pignatelli et al., 2017). NWA 12563 alteration is difficult to categorize on the CM2 scale of Rubin et al. (2007) because of the lack of tochilinite and cronstedtite. Using the scale of Velbel et al. (2015) we find that NWA 12563 would be stage 1 based on olivine and metal alteration level. The most striking feature of NWA 12563 is the abundance of magnetite, a phase associated with heavy alteration, along with the surviving primary phases olivine and porous amorphous silicate (associated with small (<100nm) nanosulfides). Magnetite is anomalously abundant from the perspective of CM2 chondrites and indicates significantly different alteration conditions (temperature, fO_2, and/or fluid compositions, etc...) for NWA 12563.

4.2 A cluster of ungrouped C2 chondrites

In Table 5 we note similarities to type 2 ungrouped chondrites (as defined in Fig. 2) as well as significant differences from CM2 chondrites. Oxygen isotopic compositions are indicators of both provenance and processing, and similar alteration processes in chondrites may lead to overlap of taxonomic classes. In this case mineral abundances and in particular the dominant Fe-rich mineral, kamacite, tochilinite or magnetite, is also a useful criterion. Ungrouped chondrites like Bells and Tagish Lake all contain ~10% magnetite (Table 5), whereas Watson et al. (1975) noted that nine tochilinite-rich CM chondrites contain <1 wt.% magnetite, and Type 1 CMs have ~3% (King et al., 2017); more pristine ungrouped chondrites like Acfer 094 are kamacite-rich. Using the oxygen isotope data base and chondrite nomenclature of Greenwood et al. (2020), we plotted the ungrouped and major group chondrites. The well-defined distribution for CM chondrites overlaps slightly with those of CO and CV chondrites and is distinct from the other coherent groups in Fig. 2. The type 2 ungrouped chondrites divide into two clusters, C2-ung1 and C2-ung2, at either end of the CM O isotope distribution. Clayton and Mayeda (1999b) had already noted that three of the C2-ung1 cluster (Bells, Essebi, and Niger I) were distinct, calling them “CI2?” chondrites. Rochette et al. (2008) proposed a new association of ungrouped chondrites with high magnetic susceptibility (i.e., high kamacite or magnetite content) including Bells, Essebi, and Acfer 094. We plot magnetic susceptibility log χ against $\delta^{18}O$ (Fig. 22) and show that the magnetite- and ^{18}O-rich cluster C2-ung 1 (Table 5), is separated from the field of CM chondrites. The kamacite-rich chondrites like Acfer 094 plot in a cluster (C2-ung 2) poor in ^{18}O overlapping the CM and CO chondrite fields.

Table 5. Alteration minerals and properties of seven cluster C2-ung1 and other chondrites.

	Bells	Essebi	NWA 12563	Niger I	WIS 91600	Tagish Lake	MET 00432	CI Orgueil	CM2 Murchison	CY (heated)
Metal	~alt	~alt	pse	pse	pse	Pse			0.16	K+T
Phyllo	s+s	s+s	s+s		dehyd	s+s	sap	s+s	s+cr	dehyd
TCI	none	none	none	none	none	None	none	none	15-40%	none
Magt	4-11	5-11	6.8	fr	6-8	Fr	fr	11	1.1	fr
Sulfide	fg	fg	ros		ros	Ros				
$\delta^{18}O$	9.59	11.65	12.60	14.5	17.1	18.5	14-18	16.16	7.3	21.97
log χ	4.82	4.85	4.67	4.89	4.78	4.94		4.78	3.86	
M_S *			6.26	9.85		9.90		9.55	0.67	3.96*
C wt.%	1.91	3.1	2.13	2.75		4.1/2.1		3.5/3.4	2.1/2.31	1.42
δ13C ‰	-19.9	-0.6	-12.2			13.4/4.7		-14.7/-12.9	-2.9/-2.4	-5.27
N(wt.%	0.064	0.137	0.095					0.149	0.105	0.075
H wt.%	0.559	0.938	0.725			0.85/0.43		1.56/0.93	1.07/0.83	0.792
δD ‰	305	337	-57.5			374/442		83.9/138	-61.7/-74.9	-102.35
C/H (at)	0.26	0.28	0.25			0.40/0.43		0.19/0.30	O.16/0.23	O.15
C_{IOM} wt%	0.96	1.30			2.26	2.00		2.00	1.06	
Refs	abdio	abeijmo	c	abcf	abdhmnp	Abgkmnor	p	abeilo	abijo	anqso

References: a Greenwood et al. 2020; b Rochette et al. 2008; c This work; d Brearley 1995, 2004; e Buseck & Hua 1993; f Desnoyer et al. 1980; g Grady et al., 2002; h Hanna et al. 2020; i Hyman and Rowe 1985,1986; j Rubin et al. 2007; k Takayama and Tomeoka 2012; l Tomeoka & Buseck 1988; m Zolensky 1991, 2002; n Tonui et al. 2014; o Alexander et al. 2012/Vacher et al. 2020; p Nakamura et al. 2013 and Yamanobe et al. 2018; q King et al., 2019; r Bischoff et al. (2020); s Gattacceca et al., 2018. Abbreviations: ~alt – partly altered; pse – pseudomorphs K+T – kamacite+ taenite; phyllo – phyllosilicate; s+s – serpentine + saponite; dehyd dehydrated; sap – saponite, s+cr – serpentine + cronstedtite; TCI tochilinite + cronstedtite; fr – framboids; fg fine grained; ros – rosettes. * Am^2/kg. The magnetic properties for CY chondrites are for Dhofar 2066.

The other chondrites in the C2-ung1 cluster also lack tochilinite like NWA 12563 (Table 5). WIS 91600 (Brearley, 2004), Niger I, and Tagish Lake (Takayama and Tomeoka, 2012) also contain serpentine pseudomorphs after kamacite. Similar ovoids are seen in chondrule rims in CR chondrites (Weisberg et al., 1993). Fe is present as magnetite framboids in the matrix in all four chondrites (Table 5), as well as in Bells and Essebi. The matrix in NWA 12563, CR and CI chondrites includes serpentine and saponite, as do Bells (Brearley, 1995), Essebi (Zolensky, 1991), and Tagish Lake (Zolensky et al., 2002; Takayama and Tomeoka, 2012) but that of CM chondrites contains serpentine and cronstedtite.

4.3 Alteration conditions in NWA 12563 and C2-ung1 chondrites

It is a truth universally acknowledged, that olivine surrounded by water must alter to serpentine. However, in C2 chondrites, where aqueous alteration is a required characteristic, chondrule olivine

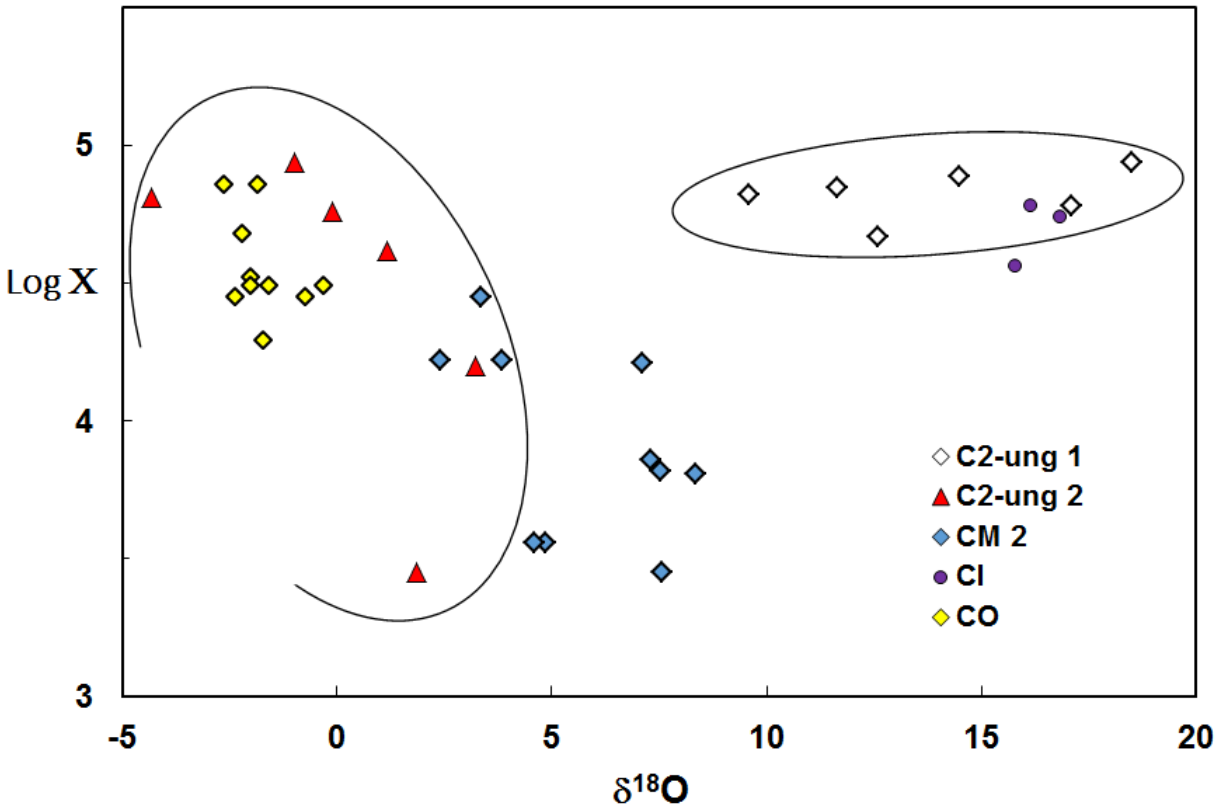

Fig. 23. In terms of magnetic susceptibility and oxygen isotopic composition, the cluster of magnetite-rich ungrouped chondrites including NWA 12563 (C2-ung1) is distinct from CM2 chondrites, while the kamacite-bearing cluster including Acfer 094 (C2-ung2) overlaps with CM2 and CO chondrites.

remains fresh except in the lowest subtypes. For example, in Nogoya, a CM2.2 chondrite (Rubin et al., 2007), chondrule phenocryst olivine is cut by veins of serpentine (Velbel et al., 2012). The lack of such veins in chondrite matrix indicates that matrix was the source of the altering fluid. The primary phases in NWA 12563 most vulnerable to alteration are amorphous silicate in the matrix, and metal and mesostasis in the chondrules. As water was probably accreted within the matrix, the extent of alteration of chondrule olivine and pyroxene may depend on the initial concentration of trapped ice, as well as on physical conditions discussed below.

In NWA 12563, chondrule mesostasis has lost Si, Al, and Ca, and gained Mg and Fe when transformed to phyllosilicates, based on Type I chondrule fresh mesostasis composition (Jones and Scott, 1989). In NWA 12563, probable sources for Mg were pyroxene when present and altered, and chondrule metal for Fe. The altered metal inclusions show a continuum of composition between kamacite and serpentine though speckled with Cr-, P-, S-rich phases (Fig. 11). Kamacite is abundant in Type I chondrules (McSween, 1977) but troilite is abundant in Type IIA chondrules (Jones, 1990). Fe lost from kamacite could be taken up by either mesostasis and by matrix, where it could eventually have contributed to magnetite precipitation. Serpentine pseudomorphs require entry of Mg and Si into chondrule metal in NWA 12563, as in WIS 91600 (Brearley, 2004). The serpentine S contents are higher than those in terrestrial serpentine, except where sulfide microinclusions are present (Debret et al., 2017), and suggest a fluid also containing S, but insufficient for forming tochilinite, unless this is strictly due to physical

858 conditions. Alteration of troilite particularly from defunct Type IIA chondrules would provide S for
859 alteration.

860 In the weakly altered CR chondrite MET 00426, alteration has begun locally in matrix: amorphous silicate
861 and nanosulfide are accompanied by nanophyllosilicate, explained by reaction after the melting of
862 interstitial ice (Le Guillou and Brearley, 2014). In Acfer 094, originally considered a CM3 chondrite
863 (Bischoff and Geiger, 1994), the matrix amorphous silicate is poor in Mg and has high $Fe^{3+}/\Sigma Fe$ ratios
864 (0.66–0.73; Hopp and Vollmer, 2018), suggesting aqueous alteration and oxidation after formation by
865 condensation. In the CR chondrites and Semarkona, the amorphous silicate phase with high Fe content and
866 high $Fe^{3+}/\sum Fe$ has been transformed during alteration to a more magnesian serpentine-saponite mixture
867 and magnetite (Le Guillou et al., 2015; Dobrica et al., 2019). In weakly altered CM chondrites the partial
868 hydration of the matrix amorphous silicate phase produces homogeneous phyllosilicate areas (Chizmadia
869 and Brearley, 2008; Hewins et al., 2014; Leroux et al., 2015; Vinogradoff et al., 2018). In NWA 12563
870 this is also observed (Fig. S5 and 17 a) are not associated with nanosulfides. The composition of matrix
871 phyllosilicate (Table 3) indicates that Fe and S were lost from amorphous silicate and nanosulfide),
872 suggesting that the larger sulfide crystals were formed at the same time.

873 Magnetite framboids precipitate from concentrated Fe-rich fluids (Yu and Kwak, 2010; Y. Kimura
874 et al, 2013) and possible sources for the Fe in NWA 12563 are amorphous silicate and metal pseudomorphs.
875 The amorphous phase in NWA 12563 has a high Fe^{3+}/Fe^{2+} ratio and has partly transformed to fibrous well-
876 ordered serpentine and saponite. Though oxidized, the amorphous silicate observed in NWA 12563 is much
877 less iron-rich than that in CRs or CMs, e.g. the amorphous silicate in Paris (Fig. 18,). This is consistent with
878 it being at least a partial source for oxidized solutions that deposited magnetite. Although magnetite
879 framboids occur in all the C2-ung1 chondrites, serpentine pseudomorphs after chondrule kamacite are
880 lacking in Bells and Essebi (Table 1) and so may not be a necessary source of the Fe in magnetite. Magnetite
881 becomes stable relative to phyllosilicates at very low pressures under conditions of low water/rock ratios
882 (Yu, 2012). Exhaustion of matrix water trapped by hydration and oxidation reactions would have caused
883 late precipitation of magnetite (and probably coarse sulfide and carbonate). Magnetite precipitation indicates
884 the exhaustion of interstitial fluid, effectively permitting the survival of amorphous silicate but also olivine.

885 The assemblages with serpentine-saponite and chlorite in NWA 12563 are reminiscent of CR
886 chondrites (Weisberg et al., 1993) rather than CM2 chondrite with tochilinite and cronstedtite. CR
887 chondrites also show replacement of metal by serpentine. In CM2 chondrites, metal is replaced by
888 tochilinite, indicating an S-rich fluid, along with P- and Cr-rich phases (Palmer and Lauretta, 2011;
889 Pignatelli et al., 2017). NWA 12563 contains magnetite framboids in chondrule rims, as well as in the
890 matrix. Magnetite also partially replaces sulfide in the rosettes. The association of dolomite with
891 magnetite seen in Fig. 19a suggests a simultaneous origin for these two phases, probably late. The
892 abundance of magnetite in NWA 12563 is anomalous relative to CI chondrites as its olivine is not altered,
893 and relative to CM chondrites as it contains no tochilinite and cronstedtite. The presence of both pyrrhotite
894 and magnetite constrains fS_2 and fO_2 to conditions well above the stability fields of kamacite and
895 tochilinite (Vacher et al., 2019). The presence of magnetite with no cronstedtite is also an indication of
896 high fO_2 and low silica activity a_{SiO2} (Palmer and Lauretta, 2011; Zolotov, 2014).

897 Temperature is clearly important in determining phase assemblages. Both saponite and chlorite
898 can be stable at high metamorphic temperatures (Iiyama and Roy, 1963; Fawcett and Yoder, 1966).
899 Amorphous silicate also seems to support relatively high temperatures, at least with low $P_{H2O,}$ since it is
900 only partially transformed to olivine at 700°C (Davoisne et al., 2006) and is abundant in the least
901 metamorphosed ordinary and CO chondrites (Dobrica et al., 2019, 2020; McAdam et al, 2018).
902 Cronstedtite is stable at low temperatures and low a_{SiO2}: Zolotov (2014) showed that cronstedtite is

replaced by magnetite and greenalite, the ferroan serpentine endmember, above about 100°C, and a metal-rich micro-region will react with local acidic fluid predominantly to magnetite (Zolotov et al., 2015). Pignatelli et al. (2017) also argued that tochilinite-cronstedtite intergrowths formed at <100 °C. However, synthesis experiments (Vacher et al., 2019) indicated that tochilinite formed from metal at 120-160°C in CM chondrites under S-bearing alkaline conditions; and cronstedtite crystals could also form from amorphous silicate and metal during later cooling (50–120°C).

Higher temperatures for NWA 12563 would be consistent with arguments that the saponite-bearing CI and C2-ung1 chondrites were altered at higher temperatures than CM chondrites considering modeling of phase equilibria (Zolensky et al., 1989) and oxygen isotope data (Clayton and Mayeda, 1999a,b). Raman spectra of organic material (Fig.21) for NWA 12563 and the CM2 chondrites Paris and Murchison (Vinogradoff et al., 2018) and therefore are not indicative of a higher temperature that could demonstrate that the stability limits for cronstedtite and tochilinite were exceeded in NWA 12563. However, temperatures based on Raman data for the organics in these meteorites are in any case poorly constrained below 220°C (Busemann et al., 2007; Quirico et al., 2018). In a similar fashion, the organic XANES data are also comparable with Paris and Murchison, which reinforces the conclusion that temperature was not significantly higher in NWA 12563. Lacking strong evidence for higher temperature, it would appear that higher fO_2, low pressure and water/rock ratio, and lower a_{SiO2} were key factors in producing abundant magnetite (Brearley, 2004; Yu, 2012; Vacher et al., 2018) in NWA 12563, as in WIS 91600, but not in CM2 chondrites.

4.4 NWA 12563 and C2-ung1 chondrite parent bodies

The textures in NWA 12563 give some clues as to the nature of its (grand) parent body. NWA 12563 is primarily very fine grained matrix, with broken, deformed, and partially rimmed chondrule fragments. It resembles regolith material. Many clusters of ferroan olivine crystals in NWA 12563 appear to be defunct Type II porphyritic chondrules (Fig. 9d) that suffered replacement of mesostasis without pseudomorphing of the chondrule. Some dispersion of the debris is possible, as suggested by Tomeoka and Buseck (1985), but the concentrations of phosphate in some defunct chondrules indicate that P from the original glass has not been transported away. The combination of small clasts (crystal clasts of unaltered olivine and chondrule fragments) with large chondrule entities (including deformed and partly disbarred chondrule shards, olivine-cluster defunct chondrules, and gerrymandered chondrules altered after fragmentation), suggests a complex history. The olivine bar segments scattered into adjacent matrix (Fig. 9b), appear consistent with chondrule fragments plunging into an unlithified, either muddy (Bland and Travis, 2017) or powdery debris matrix. If the chondrule were deformed by shocks reducing the porosity of a lithified body to the 0.7% value, the scattering of bar fragments would have been less likely. The rare isolated olivine grains in Orgueil could similarly be attributed to some kind of regolith process. The low porosity of NWA 12563 and its fractures suggest weak shocks. Could a multi-stage history, with gentle collisions during the continuing assembly of an already warmed up body, explain the unusual mineral assemblages of NWA 12563 and WIS 91600? The incorporation of unaltered chondrule debris into a warm muddy matrix would give an unusual set of conditions for alteration of high temperature phases, possibly compatible with the preservation of olivine and the serpentinization of kamacite as well as of mesostasis.

The presence of saponite suggests alteration of silica-rich phases such as glass and pyroxene, higher SiO_2 in the amorphous precursor, or higher temperature for NWA 12563 and other C2-ung1 chondrites than for CM chondrites. However, the weak 3 μm absorption and the low H abundance are not consistent with a high water content. The absence of tochilinite and cronstedtite in NWA and other C2-ung1 chondrites also suggests higher temperature. However, a higher oxygen fugacity as indicated by magnetite abundance would prevent formation of the CM chondrite phases. A combination of high temperature permitting saponite and chlorite growth coupled with exhaustion of the water and its silica content could explain the mineral assemblages in C2-ung1 chondrites.

NWA 12563 falls in the C2-ung1 cluster in Fig. 22 (Bells, Essebi, NWA 12563, Niger I, WIS 91600, and Tagish Lake, in order of increasing $\delta^{18}O$), with O isotopic compositions ranging from those of ^{18}O-rich CMs to near those of CI chondrites, but fall short of those of the heated CY (or Belgica) chondrites (Fig. 2). MET 00432 (Nakamura et al., 2013; Yamanobe et al., 2018) also has the matrix mineral assemblage and oxygen isotopic composition of this cluster, but few details are available. Among the C2-ung1 chondrites in Table 5, Bells appears to be the least altered, with fresh olivine in matrix (clasts a few tens of microns in size) and chondrules, only partly altered pyroxene, partly altered kamacite and very fine grained phyllosilicate (<1 nm to 200 nm) in the matrix (Brearley, 1995). It contains only 3.3% H_2O (Alexander et al., 2010). Despite this, Bells has been considered to be highly altered, because it is matrix-rich (McSween, 1979) and phyllosilicate-rich (Howard et al., 2015). Bells is followed by Essebi, with partially altered kamacite and pyroxene (Zolensky et al., 1991; Buseck and Hua, 1993) and WIS 91600, places third, based on kamacite pseudomorphed by serpentine though having unaltered pyroxene. NWA 12563 is like both WIS 91600 and Tagish Lake in having metal pseudomorphs, magnetite framboids, matrix saponite and also sulfide rosettes (Zolensky et al., 2002; Brearley, 2004; Tonui et al., 2014) but Tagish Lake is more altered. The gerrymandered Type I chondrules in NWA 12563 resemble chondrule cores with phyllosilicate-rich outer zones in Tagish Lake (Takayama and Tomeoka, 2012). NWA 12563 is also similar to Niger I (Table 5) but it most resembles WIS 91600.

WIS 91600 is distinct among C2-ung1 chondrites, having evidence of slight reheating. The criteria for a heating event after aqueous alteration include dehydration of phyllosilicates seen in low EMPA totals or structural changes observed in TEM, plus modification to light elements and organic material. The CY chondrite group that includes Belgica and meteorites like Yamato 86720 with very high $\delta^{18}O$ values (Tomeoka et al., 1989; Clayton and Mayeda, 1999a; King et al., 2019) has experienced some form of brief heating that caused dehydration but not recrystallization. An important question is whether heating of the parent body is due to impacts or to internal radioactivity (Sugita et al., 2019). These chondrites could alternatively have been heated by passing close to the Sun (Chaumard et al., 2012). However, peak temperature estimates for some meteorites are far above those which could be achieved by solar heating (Nakato et al., 2013).

WIS 91600 contains dehydrated saponite in the matrix (Brearley, 2004; Tonui et al., 2014). This is interpreted to be due to a milder reheating than that which produced the CY or Belgica chondrites (Tomeoka et al., 1989; Tonui et al., 2014). The bulk H values of NWA 12563 suggest affinities with heated CM chondrites (Alexander et al. (2013) though the matrix shows no evidence for desiccation of phyllosilicates (Table 3). Olivine Cr composition data show that NWA 12563 has not been reheated above stage 3.0 (Grossman and Brearley, 2005) though this method is not sensitive to heating of short duration. It is possible that NWA 12563 represents the precursor material that was slightly heated to become WIS 91600.

Harries and Langenhorst (2013) considered that Bells and Essebi are CM/CI transitional types, though this is inconsistent with δD and $\delta^{15}N$ values. Bells is also completely different from common CC chondrites except CRs in Mg isotopic composition (Van Kooten et al., 2020). NWA 12563 differs from Bells and Essebi in having sulfide rosettes, and pseudomorphed metal (Table 5) and its δD is much lower than theirs, ruling out a direct relationship. There are clearly different types of C2-ung1 chondrites, in part distinguished by different oxygen isotope compositions (Greenwood et al., 2020) plus magnetite abundance or magnetic susceptibility (Fig. 22) and none of them need be closely related to any of the CM, CI and CY chondrites. Vinogradoff et al. (2018) suggested that organic evolution before accretion into meteorite parent bodies might yield diverse organic-silicate-ice mixtures which may lead to various groups of chondrites.

4.5 NWA 12563 C2-ung1 chondrites and asteroids

Greenwood et al. (2020) have estimated the number of asteroids represented by meteorites and proposed two or three parent bodies for those in the C2-ung1 cluster: Tagish Lake plus Dho 1988 (see Fig. 2) are assigned to one parent body, with Bells and Essebi representing either one or two bodies. This approach is consistent with the large number of C-complex asteroids observed (Vernazza et al., 2017) even though many of them may not have generated NEO and probable sources of meteorites. WIS 91600 and NWA 12563 were not discussed by Greenwood et al. (2020) and could represent one or two additional parent bodies for this cluster.

Asteroid spectra resembling those of carbonaceous chondrites have a wide range of shapes, with slopes varying from negative in the visible (B class blue) to the steeply positive D class positive, with C-complex spectra having patterns between these extremes (DeMeo et al., 2009). Ungrouped carbonaceous chondrites are clearly of great interest for the interpretation of asteroid compositions, but quite similar meteorites appear to correspond to different asteroid spectral types. Direct correlation of meteorite and asteroid types may be difficult because infrared spectra are very sensitive to differences in grain size (Vernazza et al., 2016), heterogeneity (Gilmour et al., 2019), and space weathering (Brunetto et al., 2020) that may obscure details of the geologic history of the grandparent and parent bodies.

We compared the Vis-NIR spectrum of NWA 12563 with the spectral database RELAB of Brown University (www.planetary.brown.edu/relab/), using the M4AST tool at IMCCE-France (http://spectre.imcce.fr/m4ast/index.php/index/home). In terms of general spectral shape and albedo, the Vis-NIR spectrum of NWA 12563 resembles the spectra of some “bright” carbonaceous chondrites such as CO3 Frontier Mountain 95002 (see spectra in Lantz et al., 2017). The M4AST tool also provides a best match with the asteroid taxonomic class K (DeMeo et al. 2009).

We compared the MIR-FIR reflectance spectrum of NWA 12563 with the spectra of Bells and Essebi, and other carbonaceous chondrite spectra available from our previous studies (Brunetto et al. 2014, Lantz et al. 2015, Lantz et al. 2017, Brunetto et al. 2018, Noun et al. 2019) and from the literature (Hanna et al., 2020, for CM WIS 91600). In Fig. 25 we show the result of this comparison in the surface scattering range around the so called “10-μm” and “20-μm” bands (Si-O stretching and bending modes), where we also include the spectrum of asteroid Bennu (Hamilton et al. 2019). Although the peak positions of hydrated and anhydrous silicates are similar to those observed for other chondrites, the spectrum of NWA 12563 is significantly different than the spectra of the other chondrites considered here, both in terms of general shape and relative ratio between the two main peaks. It is interesting to observe how the spectral signatures of NWA 12563 and the CO3 chondrite Frontier Mountain 95002 are different, even if the two meteorites look similar in terms of Vis-NIR diffuse reflectance. This confirms that the MIR spectral range is much more diagnostic than the Vis-NIR range in terms of mineral detection and characterization. In the FIR we see that NWA12563 and WIS 91600 have similar features at 22.4 μm, and all the C2-ung1 analyzed have similar 28 μm features (Fig. 25). Generally speaking, Bells and WIS 91600 are spectrally the closest meteorites to NWA12563, since they share many similarities in peak position and overall shape.

Magnetite changes spectra from red to blue (Clark et al., 2011), yet both magnetite-rich Tagish Lake and WIS 91600 have spectra very similar to those of D-type asteroids (Hiroi et al., 2001, 2005). We

find that dispersed fine-grained magnetite may have its spectral signature obscured by other phases (Fig. 23). Tagish Lake specimens vary and match those of C-, X-, Xc-, and D-type asteroids, though not B-type (Gilmour et al., 2019). The 3 μm absorption band of WIS 91600 suggests mild heating (Tonui et al., 2014). CM2 chondrites have Ch- and Cgh-type VIR spectra, while the Bennu spectra (Hamilton et al., 2019; de Léon et al., 2018) have the negative blue B-type spectra. The Bennu spectra are spectrally ''blue'' in the VIR as in carbonaceous chondrites containing magnetite (Clark et al., 2011) and show features of phyllosilicate at ~2.7 and 23 μm, and of magnetite at 18 and 29 μm (Hamilton et al., 2019; de Léon et al., 2018). There are similarities between Bennu and some chondrites at longer wave lengths. It is significant that the 18 μm feature is also seen in Orgueil (Hamilton et al., 2019) and WIS 91600 (Hanna et al. 2020), but not in the CM2 chondrites. Thus, considering specifically magnetite, CI and C2-ung1 are possible constituents of Bennu. Our measurement on NWA 12563 indicates that the fraction of magnetite on an asteroid surface has to be extremely high to be detected in remote sensing data. If the fraction of asteroid magnetite is not as high as in NWA 12563, an unambiguous in situ detection of magnetite in localized regions of an asteroid surface would require very small footprints, difficult to be achieved by spacecraft in typical global characterization orbits. More extensive IR spectroscopy of C2-ung1 chondrites and more remote sensing spectra with smaller footprints on Bennu are needed to gain more information on asteroid properties.

Fig. 24. Comparison of the MIR and FIR reflectance spectrum of NWA 12563 with other carbonaceous chondrite spectra measured at SOLEIL (Brunetto et al. 2014, Lantz et al. 2015, Lantz et al. 2017, Brunetto et al. 2018, Noun et al. 2019) except for WIS 91600 (Hanna et al., 2020), and the spectrum of asteroid Bennu (Hamilton et al. 2019). This shows the surface scattering range around the so called "10-µm" band (Si-O stretching), with a vertical line at 1000 cm-1 (10 µm) to stress the differences in main peak position.

The spectrum of NWA 12563 also looks relatively different from the spectrum of Bennu, although some general similarities can be pointed out, such as a main peak position below 1000 cm^{-1} (above 10 µm) and a quite large width of the Si-O complex. However, the spectra of NWA 12563 and WIS 91600 in Fig. 24 give among the best matches to Bennu's spectrum. Previous experiments on irradiated chondrites (Brunetto et al. 2020) have shown that space weathering may be responsible for the spectral mismatch between Bennu and chondrites rich in hydrated matrix. We cannot exclude that irradiating NWA 12563 with low energy ions would produce a better match to Bennu's spectrum, especially because space weathering has been shown to induce a shift of the Si-O peak position towards longer wavelengths and an increase in band width.

Magnetite has been suggested to be present at the surface of Bennu (Hamilton et al. 2019), but magnetite IR features lie at higher wave lengths than the investigated spectral range for NWA 12563.

Ryugu has a smoothly rising red spectrum of the Cb-type, requiring an origin in the Eulalia or Polana family (Sugita et al., 2019; Kitazato et al., 2019). The match with the CY chondrite Y-86029 and laboratory-heated chondrites is evidence of mild heating (Sugita et al., 2019; King et al., 2019; Kitazato et al., 2019). The albedo of Ryugu is much darker than that of NWA 12563. Recently, the Hayabusa2 mission has measured the NIR spectrum of Ryugu's subsurface material within the artificial crater produced by the SCI impact experiments (Arakawa et al. 2020). The spectra collected by the NIRS3 instrument (Kitazato et al. 2020) exhibit an OH feature suggesting that the subsurface material experienced heating above 300˚C, similar to the surface. These results support the hypothesis that primary thermal alteration occurred due to radiogenic and/or impact heating on Ryugu's parent body. Unfortunately, an MIR spectrum of Ryugu is not available for now.

NEO sources of C2 chondrites are rubble piles, and it has recently been confirmed that Ryugu and Bennu are not monomict assemblages, but polymict like Almahata Sitta (Bischoff et al., 2010; Sugita et al., 2019; Tatsumi et al., 2020; Dellagiustina et al, 2020). Even if there are no foreign inclusions in an asteroid there might be fragments of different parts of the grandparent asteroid with different alteration of metamorphic histories. Asteroids may have separated into icy crusts and zones with different amounts of aqueous alteration (Castillo-Rodriguez and Schmidt (2010). Individual meteorites with different IR spectra could be derived from the same main belt asteroid, if it had a cold surface layer over a uniformly heated interior. We have concluded that NWA 12563 is a proxy for the unheated precursor to WIS 91600 and we suggest that NWA 12563 and WIS 91600 could be derived from the same grandparent body.

5. **CONCLUSIONS**

NWA 12563 contains 14% Type I and II chondrules similar in primary mineralogy to those in CM2 chondrites. However, its alteration differs: chondrule mesostasis contains serpentine-saponite and chlorite, metal is pseudomorphed by serpentine; matrix contains amorphous silicate, serpentine-saponite, plus 6.8% magnetite framboids. Cronstedtite and tochilinite are absent, possibly because of higher fO_2, lower A_{SiO2}, and higher temperature than for CM2 chondrites.

The 86% matrix contains amorphous silicate and phyllosilicate with an $Fe^{3+}/\sum Fe$ ratio measured using STXM of ~ 75 % (±5), as in most CR chondrites, Acfer 094 and Semarkona. The amorphous silicate phase, about half transformed to more magnesian serpentine-saponite, contains pores and pyrrhotite

inclusions. It is more magnesian than amorphous silicate in CR chondrites and the Paris CM2 chondrite, possibly because Fe was extracted to deposit magnetite.

NWA 12563 has similarities to a number of ungrouped magnetite-rich and ^{18}O-rich chondrites (Bells, Essebi, NWA 12563, Niger I, WIS 91600, Tagish Lake, Dho 1988 and MET 00432). We call this ^{18}O-rich cluster C2-ung1 as opposed to a second ^{18}O-poor cluster of C2 ungrouped chondrites. The C2-ung1 meteorites fall in a field on a plot of magnetic susceptibility log χ against δ^{18}O that is separated from the field for CM2 chondrites. Alteration is similar for chondrites in this cluster: there is evidence of saponite in the matrix, they lack tochilinite and cronstedtite, and magnetite is abundant; in many sulfide forms rosettes and metal is pseudomorphed by serpentine. Bells and Essebi differ slightly in having some fresh metal and no sulfide rosettes, and they also have significantly different δ^{13}C.

We agree with Greenwood et al. (2020) that the C2-ung1chondrites require several different parent bodies. NWA 12563 and WIS 91600, however, are very similar and may represent one such body. WIS 91600 has suffered dehydration of phyllosilicates and comes from the more heated portion of this body.

The Vis-NIR spectrum of NWA 12563 matches the asteroid taxonomic class K and resembles that of CO3 FRO 95002 The MIR reflectance spectrum is significantly different those of other chondrites including FRO 95002. This confirms that the MIR spectral range is much more diagnostic for mineral detection and characterization than the Vis-NIR range. Bells and WIS 91600 are spectrally the closest meteorites to NWA12563, since they share many similarities in peak position and overall shape. The identification of magnetite in Bennu means that more extensive IR spectroscopy of the magnetite-rich C2-ung1 chondrites is desirable, though an unambiguous in-situ detection of magnetite in localized regions of an asteroid surface would require very small footprints

Acknowledgments We are indebted to L. Labenne for the sample; to M. Fialin and N. Rividi for help with the electron probe; and to M.J. Carr for IGPET. This work was partly supported by the Programme National de Planétologie (PNP) of CNRS/INSU, co-funded by CNES, as well as ISITE ULNE (Université Lille Nord Europe) and the MEL (Métropole Européenne de Lille). The electron microscopy work was done at the electron microscope facility at the University of Lille with the support of the Chevreul Institute, the European FEDER and Région Hauts-de-France. We thank David Troadec for the high-quality FIB sections, partly supported by the French RENATECH network. PMZ, HL and CLG thank Ahmed Addad and Maya Marinova for their assistance with the electron microscope instruments. Light element analysis was supported by the Agence Nationale de la Recherche grant ANR-19-CE31-0027-01 HYDRaTE (PI Laurette Piani). The visible-NIR spectral measurements were supported by ANR RAHIIA_SSOM and the P2IO LabEx (ANR-10-LABX-0038) in the framework Investissements d'Avenir (ANR11-IDEX-0003-01). We are grateful to C. Sandt and F. Borondics for their precious help and support at the SMIS beamline. We thank C. Lantz and D. Baklouti for providing IR data and for discussion and R.D. Hanna for sharing the IR spectrum of WIS 91600. This work was funded by the Centre National d'Etudes Spatiales (CNES-France, Hayabusa2 mission). X-CT data were collected at the SOLEIL Synchrotron, funded through proposal no. 20160863.

REFERENCES

Abreu N. M. and Brearley A. J. (2010) Early solar system processes recorded in the matrices of two highly pristine CR3 carbonaceous chondrites, MET 00426 and QUE 99177. *Geochim. Cosmochim. Acta*, 74, 1146-1171.

Alexander C. O. D., Newsome S. D., Fogel M. L., Nittler L. R., Busemann H. and Cody, G. D. (2010) Deuterium enrichments in chondritic macromolecular material—Implications for the origin and evolution of organics, water and asteroids. *Geochim. Cosmochim. Acta* 74, 4417-4437.

Alexander C. M. O'D., Bowden R., Fogel M. L., Howard K. T., Herd C. D. K. and Nittler L. R. (2012) The provenances of asteroids, and their contributions to the volatile inventories of the terrestrial planets. *Science* 337 721–723.

Alexander C. M. O'D., Howard K. T., Bowden R. and Fogel M. L. (2013) The classification of CM and CR chondrites using bulk H, C and N abundances and isotopic compositions. *Geochim. Cosmochim. Acta* 123, 244-260.

Alexander C. M. O'D., Greenwood R. C., Bowden R., Gibson J. M., Howard K. T. and Franchi I. A. (2018) A multi-technique search for the most primitive CO chondrites. *Geochim. Cosmochim. Acta* 221, 406–420.

Berlin J., Jones R. H. and Brearley A. J. (2011) Fe-Mn systematics of type IIA chondrules in unequilibrated CO, CR, and ordinary chondrites. *Meteorit. Planet Sci.* 46, 513-533.

Bernard S., Beyssac O. and Benzerara K. (2008) Raman mapping using advanced line-scanning systems: geological applications. *Appl. Spectrosc.* 62, 1180-1188.

Beyssac O., Brunet F., Petitet J. P., Goffé B. and Rouzaud J. N. (2003) Experimental study of the microtextural and structural transformations of carbonaceous materials under pressure and temperature. *Eur. J. Mineral*. 15, 937-951.

Bischoff A. and Geiger T. (1994) The unique carbonaceous chondrite Acfer 094 The first CM3 chondrite (?). *Lunar Planet. Sci.* **XXV,** 115-116.

Bischoff A., Horstmann M., Pack A., Laubenstein M. and Haberer S. (2010) Asteroid 2008 TC3—Almahata Sitta: A spectacular breccia containing many different ureilitic and chondritic lithologies. *Meteorit. Planet Sci.*, 45, 1638-1656.

Bischoff et al. (2020) The old, unique C1 chondrite Flensburg – Insight into the first processes of aqueous alteration, brecciation, and the diversity of water-bearing parent bodies and lithologies. *Geochim. Cosmochim. Acta* doi 10.1016/j.gca.2020.10.014

Bland P. A. and Travis B. J. (2017) Giant convecting mud balls of the early solar system. Sci. Adv.3, e1602514

Bonal L. Quirico E., Bourot-Denise M. and Montagnac G. (2006) Determination of the petrologic type of CV3 chondrites by Raman spectroscopy of included organic matter. *Geochim. Cosmochim. Acta* , 70, 1849-1863.

1186 Bonal L., Bourot-Denise M., Quirico E., Montagnac G., and Lewin E. (2007) Organic matter and
1187 metamorphic history of CO chondrites. *Geochim. Cosmochim. Acta* 71, 1605-1623.

1188 Bourdelle F., Benzerara K., Beyssac O., Cosmidis J., Neuville D. R., Brown G. E., and Paineau E. (2013)
1189 Quantification of the ferric/ferrous iron ratio in silicates by scanning transmission X-ray microscopy at
1190 the Fe L 2, 3 edges. *Contrib. Mineral. Petr.*, *166*, 423-434.

1191 Brearley A.J., 1995. Aqueous alteration and brecciation in Bells, an unusual, saponite-bearing, CM
1192 chondrite. *Geochim. Cosmochim. Acta 59,* 2291-2317.

1193 Brearley A.J. (2004) A unique style of alteration of iron-nickel metal in WIS91600, an unusual C2
1194 carbonaceous chondrite. *Lunar Planet. Sci.* XXXV Abstract #1358.

1195 Brunetto R., Lantz C., Ledu D., Baklouti, D., Barucci, M.A., Beck, P., Delauche, L., Dionnet Z., Dumas
1196 P., Duprat J., Engrand C., Jamme F., Oudayer P., Quirico E., Sandt, C.E. D (2014) Ion irradiation of
1197 Allende meteorite probed by visible, IR, and Raman spectroscopies. *Icarus* 237 278–292.

1198 Brunetto R., Lantz C., Nakamura T., Baklouti D., Le Pivert-Jolivet T., Kobayashi S. and Borondics F.
1199 (2020) Characterizing irradiated surfaces using IR spectroscopy. *Icarus* 113722.

1200 Burbine T. H. 1998. Could G-class asteroids be the parent bodies of the CM chondrites? *Meteorit. Planet.*
1201 *Sci.* 33, 253-258.

1202 Buseck P. R. and Hua X. (1993) Matrices of carbonaceous chondrite meteorites. *Annu. Rev. Earth Pl. Sc.*
1203 21, 255-305.

1204 Busemann H., Alexander M. O. D. and Nittler L. R. (2007) Characterization of insoluble organic matter in
1205 primitive meteorites by microRaman spectroscopy. *Meteorit. Planet. Sci.* 42, 1387-1416.

1206 Castillo-Rogez J. C., and Schmidt B. E. (2010) Geophysical evolution of the Themis family parent body.
1207 *Geophys. Rev. Lett*. 37(10).

1208 Changela H. G., Le Guillou C., Bernard S. and Brearley A. J. (2018) Hydrothermal evolution of the
1209 morphology, molecular composition, and distribution of organic matter in CR (Renazzo-type)
1210 chondrites. *Meteorit. Planet. Sci. 53*, 1006-1029.

1211 Chaumard N., Devouard B., Delbo M., Provost A. and Zanda B. (2012) - Radiative heating of
1212 carbonaceous near-Earth objects as a cause of metamorphism for CK carbonaceous chondrites. *Icarus*
1213 220, 65-73.

1214 Chizmadia L. J. and Brearley A. J. (2008) Mineralogy, aqueous alteration, and primitive textural
1215 characteristics of fine-grained rims in the Y-791198 CM2 carbonaceous chondrite: TEM observations
1216 and comparison to ALHA81002. *Geochim. Cosmochim. Acta* 72, 602-625.

1217 Clark B. E., Binzel R. P., Howell E. S., Cloutis E. A., Ockert-Bell M., Christensen P., Barucci M. A.,
1218 DeMeo F., Lauretta D. S., Connolly H., Soderberg A., Hergenrother C., Lim L., Emery J. and
1219 Soderberg, A. (2011) Asteroid (101955) 1999 RQ36: Spectroscopy from 0.4 to 2.4 μm and meteorite
1220 analogs. *Icarus* 216, 462-475.

1221 Clayton R. N., and Mayeda T. K. (1999a) Oxygen isotope studies of carbonaceous chondrites. *Geochim.*
1222 *Cosmochim. Acta* 63, 2089-2104.

Clayton, R. N., & Mayeda, T. K. (1999b). Links among CI and CM chondrites. *Lunar Planet. Sci.* XXX abstract #1795.

Consolmagno G.J., Britt D.T., Macke R.J. 2008. The significance of meteorite density and porosity. Chemie der Erde 68:1-29.

Cournède C., Gattacceca J., Gounelle M., Rochette,P., Weiss B. P., and Zanda B. (2015) An early solar system magnetic field recorded in CM chondrites. *Earth Planet. Sci. Lett*, 410, 62-74.

Craig J. R. 1973. Pyrite-pentlandite assemblages and other low temperature relations in the Fe-Ni-S system. *Amer. J. Sci.* 273-A, 496– 510.

Davidson J., Alexander C. M. O. D., Stroud R. M., Busemann H. and Nittler L. R. (2019) Mineralogy and petrology of Dominion Range 08006: A very primitive CO3 carbonaceous chondrite. *Geochim. Cosmochim. Acta* 265, 259–278.

Davoisne C., Djouadi Z., Leroux H., d'Hendecourt L., Jones A., and Deboffle D. (2006) The origin of GEMS in IDPs as deduced from microstructural evolution of amorphous silicates with annealing. *Astron. Astrophys*. 448(1), L1-L4.

De la Peña F., Ostasevicius T., Fauske V. T., Burdet P., Jokubauskas P., Nord M., . . . Chang H.-W. (2017, 5) hyperspy/hyperspy: HyperSpy 1.3. doi:10.5281/zenodo.583693

De León J., Campins H., Morate, D., De Prá M., Alí-Lagoa V., Licandro J., ... and Popescu M. (2018) Expected spectral characteristics of (101955) Bennu and (162173) Ryugu, targets of the OSIRIS-REx and Hayabusa2 missions. *Icarus*, 313, 25-37.

Debret B., Andreani M., Delacour A., Rouméjon S., Trcera N. and Williams H. (2017) Assessing sulfur redox state and distribution in abyssal serpentinites using XANES spectroscopy. *Earth Planet. Sci. Lett*. 466, 1-11.

DellaGiustina, D. N.; Kaplan, H. H.; Simon, A. A.; Bottke, W. F.; Avdellidou, C.; Delbo, M.; Ballouz, R. -L.; Golish, D. R.; Walsh, K. J.; Popescu, M.; Campins, H.; Barucci, M. A.; Poggiali, G.; Daly, R. T.; Le Corre, L.; Hamilton, V. E.; Porter, N.; Jawin, E. R.; McCoy, T. J.; Connolly, H. C. (20Exogenic Basalt on Asteroid (101955) Bennu. Nat. Astron

DeMeo F. E., Binzel R. P., Slivan S. M., and Bus S. J. (2009) An extension of the Bus asteroid taxonomy into the near-infrared. *Icarus*, 202, 160-180.

Desnoyers C. (1980) The Niger (I) carbonaceous chondrite and implications for the origin of aggregates and isolated olivine grains in C2 chondrites. *Earth Planet. Sci. Lett*. 47, 223-234.

Dionnet Z., Suttle M., Longobardo A., Folco L., Rotundi A., Della Corte V. and King A. (2020) X-ray Computed Tomography: morphological and porosity characterization of giant Antarctic micrometeorites, *Meteorit. Planet. Sci.* 55, 1581-1599.

Dobrică E., and Brearley A. J. (2020) Amorphous silicates in the matrix of Semarkona: The first evidence for the localized preservation of pristine matrix materials in the most unequilibrated ordinary chondrites. *Meteorit. Planet. Sci.* 55, 649-668.

Dobrică E., Le Guillou C. and Brearley A. J. (2019) Aqueous alteration of porous microchondrules in Semarkona: Implications for hydration, oxidation and elemental exchange processes. *Geochim. Cosmochim. Acta* 244, 292-307.

Fawcett J.J. and Yoder H.S., Jr. (1966) Phase relationships of chlorites in the system MgO-Al_2O_3-SiO_2-H_2O. *Amer. Mineral.* 51, 353-380.

Gattacceca J., Suavet C., Rochette P., Weiss B. P., Winklhofer M., Uehara M. and Friedrich J. M. (2014) Metal phases in ordinary chondrites: Magnetic hysteresis properties and implications for thermal history. *Meteorit. Planet. Sci.* 49, 652-676.

Gattacceca J., Bouvier A., Grossman J., Metzler K., Uehara M. 2018. The Meteoritical Bulletin, No. 106. *Meteorit. Planet. Sci.* 54:469-471. doi 10.111/maps.13215

Gilmour C. M., Herd C. D., and Beck P. (2019) Water abundance in the Tagish Lake meteorite from TGA and IR spectroscopy: Evaluation of aqueous alteration. *Meteorit. Planet. Sci.* 54(9), 1951-1972.

Grady M. M., Verchovsky A. B., Franchi I. A., Wright I. P. and Pillinger C. T. (2002) Light dement geochemistry of the Tagish Lake CI2 chondrite: Comparison with CI1 and CM2 meteorites. *Meteorit. Planet. Sci.* 37, 713-735.

Greenwood R. C., Burbine T. H. and Franchi I. A. (2020) Linking asteroids and meteorites to the primordial planetesimal population. *Geochim. Cosmochim. Acta*, 227, 377-406.

Greshake, A. (1997) The primitive matrix components of the unique carbonaceous chondrite Acfer 094: A TEM study. *Geochim. Cosmochim. Acta* 61, 437-452.

Grossman J. N. and Brearley A. J. (2005) The onset of metamorphism in ordinary and carbonaceous chondrites. *Meteorit. Planet. Sci.* 40, 87–122.

Gursoy D., De Carlo F., Xiao X., and Jacobsen C. 2014. Tomopy: A framework for the analysis of synchrotron tomographic data. Journal of Synchrotron Radiation 21,1188–1193.

Hamilton, V. E., Simon, A. A., Christensen, P. R., Reuter, D. C., Clark, B. E., Barucci, M. A., ... and Connolly, H. C. (2019) Evidence for widespread hydrated minerals on asteroid (101955) Bennu. *Nature astronomy* 3(4), 332-340.

Hanna, R. D., Hamilton, V. E., Haberle, C. W., King, A. J., Abreu, N. M., and Friedrich, J. M. (2020) Distinguishing relative aqueous alteration and heating among CM chondrites with IR spectroscopy. *Icarus* 113760.

Hanowski N. P. and Brearley A. J. (2001) Aqueous alteration of chondrules in the CM carbonaceous chondrite, Allan Hills 81002: implications for parent body alteration. *Geochim. Cosmochim. Acta* 65, 495–518.

Harju E. R., Rubin A. E., Ahn I., Choi B. G., Ziegler K. and Wasson J. T. (2014) Progressive aqueous alteration of CR carbonaceous chondrites. *Geochim. Cosmochim. Acta* 139, 267-292.

Harries D. and Langenhorst F. 2013. The nanoscale mineralogy of Fe, Ni sulfides in pristine and metamorphosed CM and CM/CI-like chondrites: Tapping a petrogenetic record. *Meteorit. Planet. Sci.* 48, 879-903.

Hewins R. H., Bourot-Denise M., Zanda B., Leroux H., Barrat J.-A., Humayun M., Göpel C., Greenwood R. C., Franchi I. A., Pont S., Lorand J.-P., Cournède C., Gattacceca J., Rochette P., Kuga M., Marrocchi Y. and Marty B. (2014) The Paris meteorite, the least altered CM chondrite so far. *Geochim. Cosmochim. Acta* 24, 90–222.

Hiroi T., Zolensky M. E., and Pieters C. M. (2001) The Tagish Lake meteorite: A possible sample from a D-type asteroid. *Science* 293(5538), 2234-2236.

Hopp T. and Vollmer C. (2018) Chemical composition and iron oxidation state of amorphous matrix silicates in the carbonaceous chondrite Acfer 094. *Meteorit. Planet. Sci.53*(2), 153-166.

Howard K. T., Alexander C. O. D., Schrader D. L. and Dyl K. A. (2015) Classification of hydrous meteorites (CR, CM and C2 ungrouped) by phyllosilicate fraction: PSD-XRD modal mineralogy and planetesimal environments. *Geochim. Cosmochim. Acta* 149, 206-222.

Hyman M. and Rowe M.W., (1986) Saturation magnetization measurements of carbonaceous chondrites. *Meteoritics, 21*, 1-22.

Hyman M., Ledger E.B. and Rowe M.W., 1985. Magnetite morphologies in the Essebi and Haripura CM chondrites. *J. Geophys. Res-Solid 90*(S02), C710-C714.

Iiyama J. T. and Roy R. (1963) Unusually stable saponite in the system Na_2O-MgO-Al_2O_3-SiO_2. *Clay Miner. Bull.* 5(29), 161-171.

Ikeda Y. (1983) Alteration of chondrules and matrices in the four Antarctic carbonaceous chondrites ALH-77307 (C3), Y-790123 (C2), Y-75293 (C2), and Y-74662 (C2) *Mem. Natl. Inst. Polar Res. Special Issue* 30, 93-108.

Jones R. H. 1990. Petrology and mineralogy of type II, FeO-rich chondrules in Semarkona (LL3.0): Origin by closed system fractional crystallization, with evidence for supercooling. *Geochim. Cosmochim. Acta* 54, 1785–1802.

Jones R. H. and Scott E. R. D. (1989) Petrology and thermal history of type IA chondrules in the Semarkona (LL3.0) chondrite. *Proc.19th Lunar Planet. Sci. Conf.*, 523-536.

Ketcham R. A., 2005. Three-dimensional grain fabric measurements using high-resolution X-ray computed tomography. *J. Struct. Geol*. 27, 1217–1228.

Kimura M., Grossman, J. N., and Weisberg, M. K. (2011) Fe-Ni metal and sulfide minerals in CM chondrites: An indicator for thermal history. *Meteorit. Planet. Sci.* 46(3), 431-442.

Kimura M., Imae N., Yamaguchi A., Greenwood R. C., Komatsu M. and Noguchi T. (2019) Primitive CM-related chondrites: their characteristic features and classification. In *82nd Annual Meeting of The Meteoritical Society*, Abstract #6042.

Kimura Y., Sato T., Nakamura N., Nozawa J., Nakamura T., Tsukamoto K. and Yamamoto K.(2013) Vortex magnetic structure in framboidal magnetite reveals existence of water droplets in an ancient asteroid. *Nature Communications*, *4*(1), 1-8.

King A.J., Schofield P.F. and Russell S.S., 2017. Type 1 aqueous alteration in CM carbonaceous chondrites: implications for the evolution of water-rich asteroids. *Meteorit. Planet. Sci.* 52, 1197–1215.

King A. J., Bates H. C., Krietsch D., Busemann H., Clay P. L., Schofield P. F. and Russell, S. S. (2019) The Yamato-type (CY) carbonaceous chondrite group: Analogues for the surface of asteroid Ryugu? *Geochemistry* 79, 125531.

Kitazato K., Milliken R. E., Iwata T., Abe M., Ohtake M., Matsuura S., ... and Senshu H. (2019) The surface composition of asteroid 162173 Ryugu from Hayabusa2 near-infrared spectroscopy. *Science* 364, 272-275.

Krot A. N., Petaev M. I., Russell S. S., Itoh S., Fagan T. J., Yurimoto, H., Chizmadia L., Weisberg M. K., Komatsu M., Ulyanov A. A. and Keil K. (2004) Amoeboid olivine aggregates and related objects in carbonaceous chondrites: records of nebular and asteroid processes. *Geochemistry* 64, 185-239.

Lanari P., Vidal O., De Andrade V., Dubacq B., Lewin E., Grosch E. G. and Schwartz S. (2014) XMapTools: A MATLAB©-based program for electron microprobe X-ray image processing and geothermobarometry. *Computers and Geosciences, 62*, 227-240. doi:10.1016/j.cageo.2013.08.010

Lappe S. C. L., Church N. S., Kasama T., da Silva Fanta A. B., Bromiley G., Dunin-Borkowski R. E., Feinberg J. M., Russell S. and Harrison R. J. (2011) Mineral magnetism of dusty olivine: a credible recorder of pre-accretionary remanence. *Geochemistry, Geophysics, Geosystems* 12(12).

Lauretta D. S., Al Asad M., M., Ballouz R. L., Barnouin O. S., Bierhaus E. B., Boynton W. V., Breitenfeld L. B., Calaway M. J., Chojnacki M., Christensen P. R., Clark B. E., Connolly H. C., d'Aubigny C. D., Daly M. G., Daly R. T., Delbo M., DellaGiustina D. N., Dworkin J. P., Emery J. P., Enos H. L., Farnocchia D., Golish D. R., Haberle C. W., Hamilton V. E., Hergenrother C. W., Jawin E. R., Kaplan H. H., Le Corre L., McCoy T. J., McMahon J. W., Michel P., Molaro J. L., Nolan M. C., Pajola M., Perry M. E., Reuter D. C., Rizk B., Roberts J. H., Ryan A., Scheeres D. J., Schwartz S. R., Simon A. A., Susorney H. C. M., Walsh K. J., Palmer E., Zou X.-D. (2019) OSIRIS-REx Arrives at Asteroid (101955) Bennu: Exploration of a Hydrated Primitive Near-Earth Asteroid. *50th Lunar and Planetary Science Conference* Abstract #2608.

Le Guillou C. and Brearley A. (2014) Relationships between organics, water and early stages of aqueous alteration in the pristine CR3.0 chondrite MET 00426. *Geochim. Cosmochim. Acta* 131, 344-367.

Le Guillou C., Bernard S., Brearley A. J. and Remusat L. (2014) Evolution of organic matter in Orgueil, Murchison and Renazzo during parent body aqueous alteration: In situ investigations. *Geochim. Cosmochim. Acta 131*, 368-392.

Le Guillou C., Changela H. G., and Brearley A. J. (2015) Widespread oxidized and hydrated amorphous silicates in CR chondrites matrices: Implications for alteration conditions and H_2 degassing of asteroids. *Earth Planet. Sci. Lett. 420*, 162-173.

Le Guillou C., Bernard S., De la Pena F. and Le Brech Y. (2018) XANES-Based Quantification of Carbon Functional Group Concentrations. *Analytical chemistry, 90*(14) 8379-8386.

Leroux H. , Cuvillier P., Zanda B. and Hewins R. (2015) GEMS-like material in the matrix of the Paris meteorite and the early stages of alteration of CM chondrites. *Geochim. Cosmochim. Acta* 70, 247–265.

Lupker M., France-Lanord C., Galy V., Lavé J., Gaillardet J., Gajurel A. P., ... and Sinha R. (2012) Predominant floodplain over mountain weathering of Himalayan sediments (Ganga basin). *Geochim. Cosmochim. Acta* 84, 410-432.

Maeda M., Tomeoka K., and Seto Y. (2009) Early aqueous alteration process in the QUE97990 and Y791198 CM carbonaceous chondrites. *J. Miner. Petrol. Sci.*104, 92-96.

McAdam M. M., Sunshine J. M., Howard K. T., Alexander C. M., McCoy T. J. and Bus S. J. (2018) Spectral evidence for amorphous silicates in least-processed CO meteorites and their parent bodies. *Icarus*, *306*, 32-49.

McSween H. Y. Jr (1977) Chemical and petrographic constraints on the origin of chondrules and inclusions in carbonaceous chondrites. *Meteorit. Planet. Sci.* 41, 1843-1860.

McSween H. Y. Jr (1979) Alteration in CM carbonaceous chondrites inferred from modal and chemical variations in matrix. *Meteorit. Planet. Sci.* 43, 1761-1770.

McSween H. Y. Jr (1987) Aqueous alteration in carbonaceous chondrites: Mass balance constraints on matrix mineralogy. *Meteorit. Planet. Sci.* 51, 2469-2477.

Mirone A., Brun E., Gouillart E., Tafforeau P. and Kieffer J. (2014) The PyHST2 hybrid distributed code for high speed tomographic reconstruction with iterative reconstruction and a priori knowledge capabilities. *Nucl. Instrum. Methods Phys. Res.*, Sect. B 324, 41-48.

Nakamura T., Noguchi T., Kimura Y., Hiroi T., Ahn I., Lee J. I. and Sasaki S. (2013) MET00432: Another Tagish Lake-type carbonaceous chondrite from Antarctica. *Meteorit. Planet. Sci.* 48, A258-A258).

Newton J., Bischoff A., Arden J. W., Franchi I. A., Geiger T., Greshake A. and Pillinger, C. T. (1995) Acfer 094, a uniquely primitive carbonaceous chondrite from the Sahara. *Meteoritics* 30, 47-56.

Nittler L. R., Alexander C. M. O'D., Davidson J., Riebe M. E. I., Stroud R. M. and Wang J. (2018) High abundances of presolar grains and 15N-rich organic matter in CO3. 0 chondrite dominion range 08006. *Geochim. Cosmochim. Acta* 226, 107–131.

Palmer E. and Lauretta D. S. (2011) Aqueous alteration of kamacite in CM chondrites. *Meteorit. Planet. Sci.* 46, 1587–1607.

Pearson V. K., Sephton M. A., Franchi I. A., Gibson J. M. and Gilmour, I. (2006) Carbon and nitrogen in carbonaceous chondrites: Elemental abundances and stable isotopic compositions. *Meteorit. Planet. Sci.* 41, 1899-1918.

Piani L., Yurimoto H. and Remusat L. (2018) A dual origin for water in carbonaceous asteroids revealed by CM chondrites. *Nature Astronomy* **2**, 317–323.

Pignatelli I., Marrocchi Y., Mugnaioli E., Bourdelle F. and Gounelle M. (2017) Mineralogical, crystallographic and redox features of the earliest stages of fluid alteration in CM chondrites. *Geochim. Cosmochim. Acta* 209, 106–122.

Quirico E., Bonal L., Beck P., Alexander C.M.O'D., Yabuta H., Nakamura T., Nakato A., Flandinet L, Montagnac G.. Schmitt-Koppling P. and Herd C.D.K. (2018) Prevalence and nature of heating processes in CM and C2-ungrouped chondrites as revealed by insoluble organic matter. *Geochim. Cosmochim. Acta* 241, 17–37.

Rochette P., Gattacceca J., Bonal L., Bourot-Denise M., Chevrier V., Clerc J.P., Consolmagno G., Folco L., Gounelle, M., Kohout T. and Pesonen, L. (2008) Magnetic classification of stony meteorites: 2. Non-ordinary chondrites. *Meteorit. Planet. Sci.* 43, 959-980.

Rowe M.W., Clayton R.N. and Mayeda T.K. (1994) Oxygen isotopes in separated components of CI and CM meteorites. *Geochim. Cosmochim. Acta* 58, 5341-5347.

Rubin A. E., Trigo-Rodrıguez J. M., Huber H. and Wasson J. T. (2007) Progressive alteration of CM carbonaceous chondrites. *Geochim. Cosmochim. Acta* 71, 2361–2382.

Sugita S., Honda R., Morota T., Kameda S., Sawada H., Tatsumi E., ... and Sakatani N. (2019) The geomorphology, color, and thermal properties of Ryugu: Implications for parent-body processes. *Science* 364.6437.

Tachibana S., Sawada H., Okamoto C., Yano H., Okazaki R., Takano Y., Miura Y. N., Sakamoto K. (2019) Hayabusa2 Touch-and-Go Sampling at Ryugu. *Lunar Planet. Sci. Conf. 50th* Abstract #1939.

Takayama A. and Tomeoka K. (2012) Fine-grained rims surrounding chondrules in the Tagish Lake carbonaceous chondrite: Verification of their formation through parent-body processes. *Geochim. Cosmochim. Acta* 98, 1-18.

Tatsumi, E., Sugimoto, C., Riu, L. et al. (2020) Collisional history of Ryugu's parent body from bright surface boulders. *Nat. Astron.* https://doi.org/10.1038/s41550-020-1179-z

Tomeoka K. and Buseck P.R. (1985) Indicators of aqueous alteration in CM carbonaceous chondrites: microtextures of a layered mineral containing Fe, S, O and Ni. *Geochim. Cosmochim. Acta* 49, 2149–2163.

Tomeoka K. and Buseck P. R. (1988) Matrix mineralogy of the Orgueil CI carbonaceous chondrite. *Geochim. Cosmochim. Acta* 52, 1627-1640.

Tomeoka K., Kojima H. and Yanai, K. (1989) Yamato-82162: A new kind of CI carbonaceous chondrite found in Antarctica. *Proc. NIPR Symp. Antarct. Meteorites* 2, 36-54.

Tonui E., Zolensky M., Hiroi T., Nakamura T., Lipschutz M. E., Wang M. S. and Okudaira K. (2014) Petrographic, chemical and spectroscopic evidence for thermal metamorphism in carbonaceous chondrites I: CI and CM chondrites. *Geochim. Cosmochim. Acta* 126, 284-306.

Tronche E. J., Hewins R. H. and MacPherson G. J. (2007) Formation conditions of aluminum-rich chondrules. *Geochim. Cosmochim. Acta* 70, 336-338.

Vacher L. G., Marrocchi Y., Verdier-Paoletti M. J., Villeneuve J. and Gounelle M. (2016) Inward radial mixing of interstellar water ices in the solar protoplanetary disk. *Astrophys. J. Lett*. 827(1), L1.

Vacher L. G., Truche L., Faure F., Tissandier L., Mosser-Ruck R. and Marrocchi, Y. (2019) Deciphering the conditions of tochilinite and cronstedtite formation in CM chondrites from low temperature hydrothermal experiments. *Meteorit. Planet. Sci.* 54, 1870-1889.

Vacher L. G., Piani L., Rigaudier T., Thomassin D., Florin G., Piralla M. and Marrocchi Y. (2020) Hydrogen in chondrites: Influence of parent body alteration and atmospheric contamination on primordial components. *Geochim. Cosmochim. Acta* 281, 53-66.

van Kooten E., Cavalcante L., Wielandt D. and Bizzarro M. (2020) The role of Bells in the continuous accretion between the CM and CR chondrite reservoirs. *Meteorit. Planet. Sci.* 55, 575-590.

Velbel M. A., Tonui E. K. and Zolensky M. E. (2012) Replacement of olivine by serpentine in the carbonaceous chondrite Nogoya (CM2). *Geochim. Cosmochim. Acta* 87, 117-1

Velbel M.A., Tonui E.K. and Zolensky M.E., (2015) Replacement of olivine by serpentine in the Queen Alexandra Range 93005 carbonaceous chondrite (CM2): Reactant–product compositional relations, and isovolumetric constraints on reaction stoichiometry and elemental mobility during aqueous alteration. *Geochim. Cosmochim. Acta* 148, 402-425.

Vernazza P. and Beck, P. 2017 Chapter 13 - Composition of Solar System Small Bodies. In *Planetesimals: Early Differentiation and Consequences for Planets*, pp 269-297, Edited by Linda T. Elkins-Tanton, Benjamin P. Weiss, Cambridge University Press.

Vernazza P., Marsset M., Beck P., Binzel R. P., Birlan M., Cloutis E. A., DeMeo F. E., Dumas C. and Hiroi T. (2016) Compositional homogeneity of CM parent bodies. *Astron. J.* 152, 54.

Vernazza P., Castillo-Rogez J., Beck P., Emery J., Brunetto R., Delbo M., Marsset M., F. Marchis, Groussin O., Zanda B., Lamy P., Jorda L., Mousis O., Delsanti A., Djouadi Z., Dionnet Z., Borondics F. and Lamy P. (2017) Different origins or different evolutions? Decoding the spectral diversity among C-type asteroids. *Astron. J.* 153(2), 72.

Vinogradoff V., Le Guillou C., Bernard S., Binet L., Cartigny P., Brearley A.J. and Remusat L. (2018) Paris vs. Murchison: Impact of hydrothermal alteration on organic matter in CM chondrites. *Geochim. Cosmochim. Acta* 212, 234-252.

Walsh K. J., Morbidelli A., Raymond S. N., O'Brien D. P. and Mandell A. M. (2011) A low mass for Mars from Jupiter's early gas-driven migration. *Nature*, *475*(7355), 206.

Warren, P. H. (2011). Stable-isotopic anomalies and the accretionary assemblage of the Earth and Mars: A subordinate role for carbonaceous chondrites. *Earth Planet. Sci. Lett*. 311, 93-100.

Watson D.E., Larson E.E., Herndon J.M. and Rowe M.W., 1975. Thermomagnetic analysis of meteorites, 2. C2 chondrites. *Earth Planet. Sci. Lett.*, *27,* 101-107.

Weisberg M.K., Prinz M., Clayton R.N. and Mayeda T.K., 1993. The CR (Renazzo-type) carbonaceous chondrite group and its implications. *Geochim. Cosmochim. Acta* 57, 1567–1586.

Yamanobe M., Nakamura T. and Nakashima D. (2018) Oxygen isotope reservoirs in the outer asteroid belt inferred from oxygen isotope systematics of chondrule olivines and isolated forsterite and olivine grains in Tagish Lake-type carbonaceous chondrites, WIS 91600 and MET 00432. *Polar Science* 15, 29-38.

Yang B. and Jewitt D. (2010) Identification of magnetite in B-type asteroids. *Astron. J. 140*(3), 692.

Yu, B. Y., and Kwak, S. Y. (2010) Assembly of magnetite nanocrystals into spherical mesoporous aggregates with a 3-D wormhole-like pore structure. *J. Mater. Chem.*, 20(38), 8320-8328.

Zanetta P.-M., Le Guillou C., Leroux H., Zanda B., Hewins R. H., Lewin E., and Pont S. (2019) Modal abundance, density and chemistry of micrometer-sized assemblages by advanced electron microscopy: application to chondrites. *Chem. Geol*. 514, 27–41.

1485 Zanetta P.-M., Leroux H., Le Guillou C., Zanda B., Hewins R. H. (2021) Fine-grained rims vs. matrix in
1486 the Paris CM chondrite. *Geochim. Cosmochim. Acta*

1487 Zolensky M. E., Bourcier W. L. and Gooding J. L. (1989) Aqueous alteration on the hydrous asteroids:
1488 Results of EQ3/6 computer simulations. *Icarus* 78, 411-425.

1489 Zolensky M. E. (1991) Mineralogy and matrix composition of "CR" chondrites Renazzo and EET 87770,
1490 and ungrouped chondrites Essebi and MAC 87300. *Meteoritics* 26, 414.

1491 Zolensky M., Barrett R. and Browning L. (1993) Mineralogy and composition of matrix and chondrule
1492 rims in carbonaceous chondrites. *Geochim. Cosmochim. Acta* 57, 3123-3148.

1493 Zolensky M. E., Nakamura K., Gounelle M., Mikouchi T., Kasama T., Tachikawa O. and Tonui E. (2002)
1494 Mineralogy of Tagish Lake: An ungrouped type 2 carbonaceous chondrite. *Meteorit. Planet. Sci.* 37,
1495 737-761.

1496 Zolotov M. Y. 2014. Formation of brucite and cronstedtite-bearing mineral assemblages on Ceres. *Icarus*
1497 228, 13–26.

1498 Zolotov, M. Y., Morlok, A., & Libourel, G. (2015). Microchemical environments of aqueous alteration in
1499 CR chondrites: chemical equilibrium models. *Lunar Planet. Sci. Conf. 50th* Abstract #11470.

1500 Zolotov M.Yu. (2012) Aqueous fluid composition in CI chondritic materials: Chemical equilibrium
1501 assessments in closed systems. *Icarus* 220, 713–729.

1502 Yu, B. Y., and Kwak, S. Y. (2010) Assembly of magnetite nanocrystals into spherical mesoporous
1503 aggregates with a 3-D wormhole-like pore structure. *J. Mater. Chem*., 20(38), 8320-8328.

1504

1505 **Electronic Annex** Supporting Material for "NWA 12563 and ungrouped C2 chondrites …"

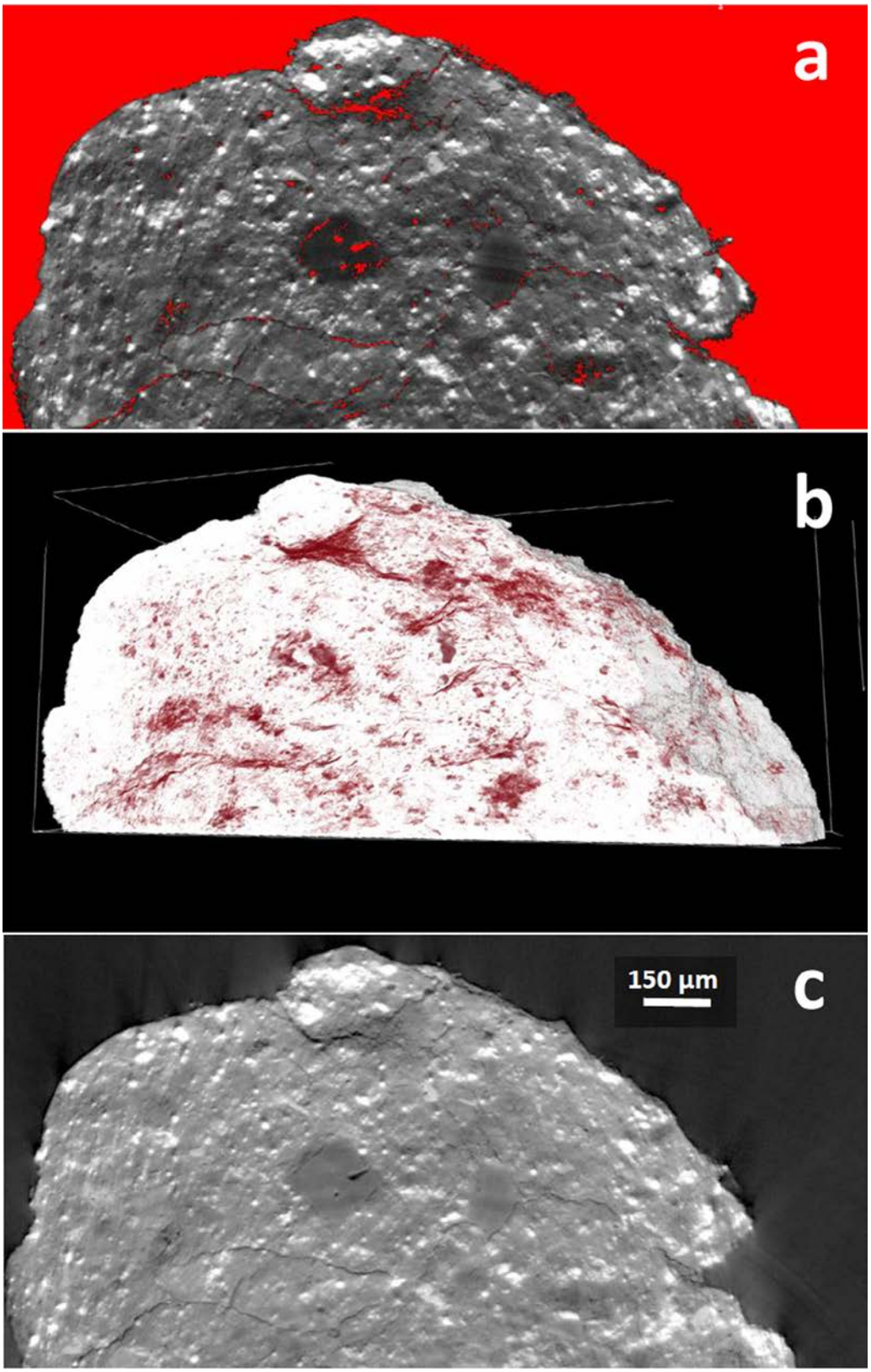

Fig. S1. X-CT images of a matrix chip showing (a) porosity in red (b) fractures in red (c) magnetite in white.

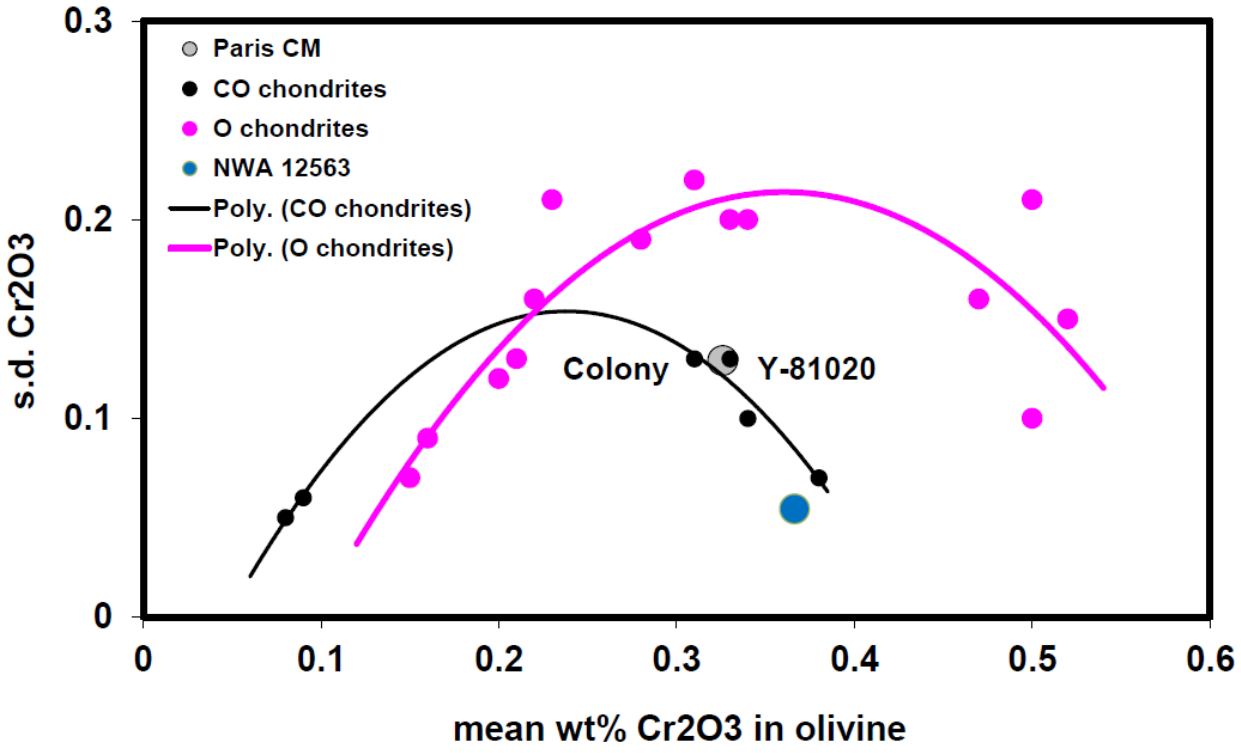

Fig. S2. Chromium diagram for ferroan olivine in NWA 12563, after Grossman and Brearley (2005). The lack of heterogeneity due to exsolution of chromite in olivine shows that the chondrules have not been significantly reheated.

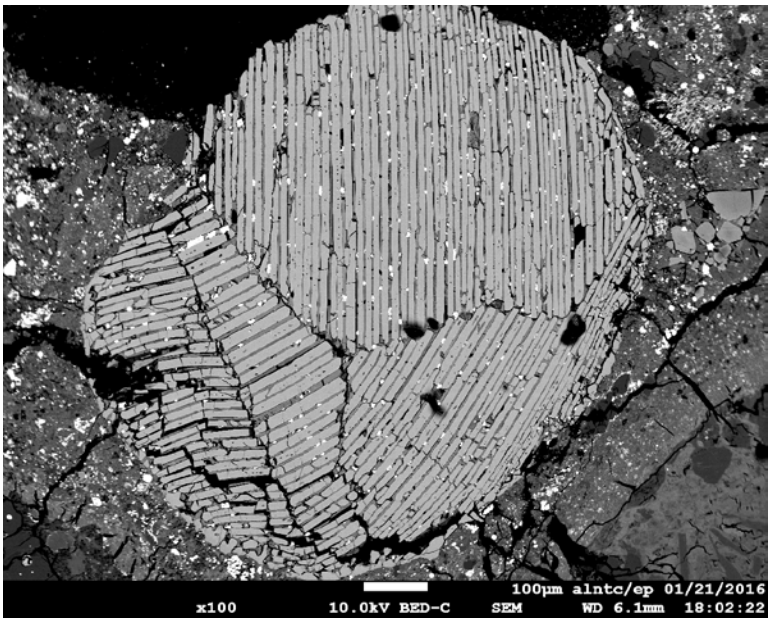

Fig. S3. Type IIA barred olivine chondrule with fractures, microfaults, and kinking.

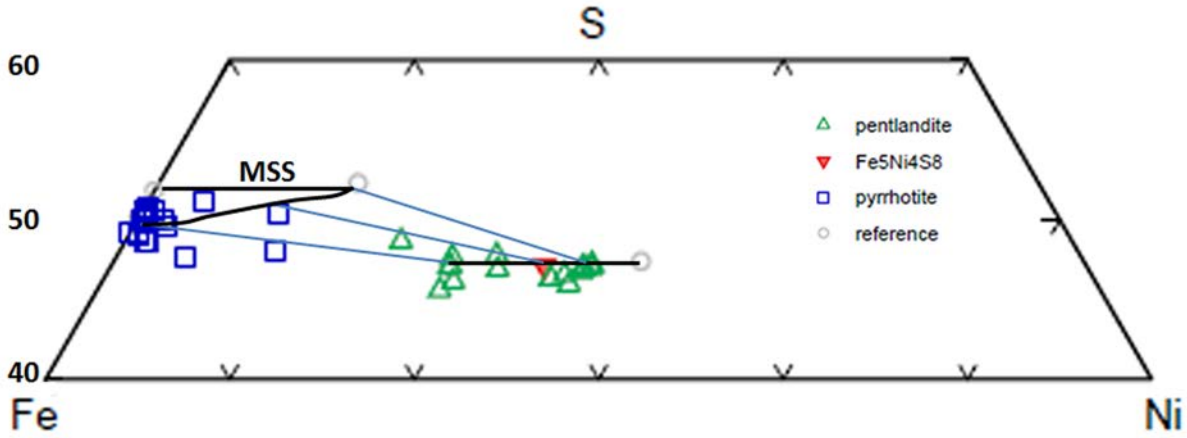

Fig. S4. Compositions of sulfides in atom % on part of the 200°C section of the Fe-NiS system, based on reference compositions from Craig (1973) and Harries and Langenhorst. (2013).

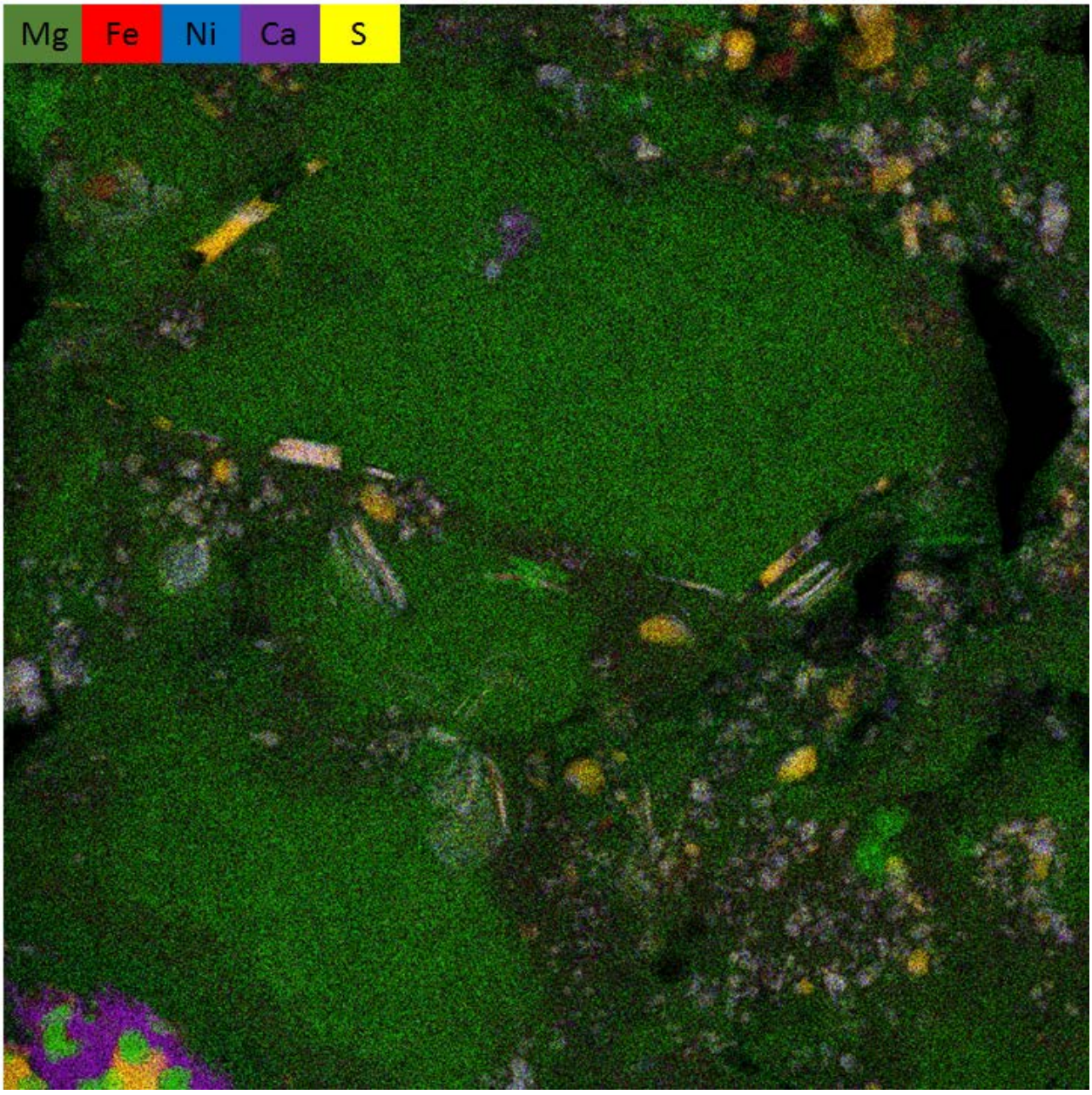

Fig. S5. An Mg-Fe-Ni-Ca-S x-ray map of the area of the matrix of NWA 12563 in Fig. 16, showing phyllosilicate-rich patches (green) and porous multi-phase regions with amorphous silicate and sulfide inclusions. Width of image ~9 μm.